IMAGING HYDRAULIC FRACTURES: SOURCE LOCATION UNCERTAINTY ANALYSIS AT THE UPRC CARTHAGE TEST SITE

Yingping Li

Earth Resources Laboratory
Department of Earth, Atmospheric, and Planetary Sciences
Massachusetts Institute of Technology
Cambridge, MA 02139

Xianhuai Zhu

Union Pacific Resources
Fort Worth, TX 76101

Arthur C. H. Cheng, and M. Nafi Toksöz

Earth Resources Laboratory
Department of Earth, Atmospheric, and Planetary Sciences
Massachusetts Institute of Technology
Cambridge, MA 02139

ABSTRACT

Hydraulic fracturing is a useful tool for enhancing gas and oil production. High-resolution seismic imaging of the fracture geometry and fracture growth process is the key in determining optimal spacing and location of wells and in improving reservoir performance for increased production rate. In this paper, we address how accurately the sources along a fracture zone at different depths can be determined for given velocity models, geophone array geometry configurations, and location of monitor wells. We apply a theory of uncertainty analysis to estimate microearthquake location uncertainties in both relative and absolute senses. To estimate the location uncertainties, we used the velocity models, two geophone arrays in two monitor wells, and the location of the fracture well, and an assumed fracture orientation of an upcoming hydraulic fracturing experiment by Union Pacific Resources Company (UPRC) and its partners at Carthage

Field, Panola, Texas.

We calculated the 95% confidence regions, in both absolute and relative senses, for five hypothetical sources along an assumed strike of a target fracture zone at three different depths. The semimajor and semiminor axes of the relative error ellipses for these epicenters are typically estimated to be 12 and 5 ft, respectively, and the relative depth uncertainty is derived at about 6 ft. The absolute location uncertainties are at least 3 to 10 times larger than the relative location uncertainties. The high-precision relative source locations result in a relative measurement error about 4-15% in measuring the fracture length. The location ambiguity from two-station locations is discussed and arrival azimuthals is proposed to to be used for removing such location ambiguity. The location uncertainty analysis is expected to be generalized as a practical tool in optimal designing of a two-well seismic monitoring system for high-resolution imaging of hydraulic fractures.

INTRODUCTION

Hydraulic fracturing has been a common engineering practice in the enhancement of gas and oil production, geothermal energy extraction, and the safe disposal of hazardous waste (Fehler *et al.*, 1987; Vinegar *et al.*, 1992; Truby *et al.*, 1994; Li *et al.*, 1995a, 1996). Understanding the fracture process and geometry is very important in designing a hydraulic fracture treatment for optimizing production efficiency from a hydrocarbon reservoir (Wills *et al.*, 1992; Zhu *et al.*, 1996). The knowledge of fracture orientation, height, and extent is essential to determine the optimal spacing and location of wells and will result in better reservoir performance in the case of both primary and secondary production.

Hydraulic fracturing often induces microearthquakes in a hydraulic fracture zone and its vicinity. Seismic monitoring techniques have been used to image the fracture geometry (House, 1987; Wills *et al.*, 1992; Phillips *et al.*, 1992; Block *et al.*, 1993; Li *et al.*, 1995a, 1996) and to reveal the fracture growth process (Li *et al.*, 1995a, 1996). The seismic imaging technique has proven to be one of the best methods for 3-D imaging and characterizing subsurface fractures and cracks. Seismic monitoring techniques trace the fracture growth process in real time and estimate the hypocentral locations of induced microearthquakes and associated location uncertainties. Microearthquakes induced by hydraulic fracturing at the Fenton Hill geothermal test site were located with an absolute location error of 30 to 40 meters (House, 1987; Phillips *et al.*, 1992; Li *et al.*, 1995a, 1996) and a relative location uncertainty of about 5 meters (Phillips *et al.*, 1992; Li *et al.*, 1995a, 1996) using seismic data recorded at four borehole stations. Vinegar *et al.* (1992) estimated the accuracy of relative location for microearthquakes induced by hydraulic fracturing in the Belridge diatomite to be less than $\pm$ 5 ft with four seismic arrays in three monitor wells. Rieven and Rodi (1995) estimated the best relative location errors to be about 3 to 8 ft for induced microearthquakes at the test site for the Deep Well Treatment and Injection (DWTI) program in Jasper, Texas, with seismic data from 96

of the 150 available geophones in two monitor wells.

To obtain a better understanding of the fracture geometry and fracture growth process in the Cotton Valley tight gas sands, Union Pacific Resources Company (UPRC) carried out a pilot study in 1994 to detect and locate microearthquakes induced by hydraulic fracturing in the Carthage Field, Panola County, Texas (Zhu *et al.*, 1996). Seismic events induced by hydraulic fracturing at a depth of 9500 ft were detectable at a distance exceeding 1300 ft in Carthage's sand and shale formations (Zhu *et al.*, 1996). Following this pilot test, a massive hydraulic fracturing experiment was proposed to be carried out at Carthage Field in 1996. One of the major goals of this experiment is to image the fracture geometry and growth process with seismic waveforms generated by microearthquakes induced by hydraulic fracturing.

In order to reliably and accurately estimate the fracture length, azimuth, and height using the high-precision source location of induced earthquakes, it is critical to analyze location errors for a given source-receiver geometry configuration. Location error analysis has been widely used in earthquake seismology for the optimal designing of seismic networks (Kijko, 1977; Uhrhammer, 1980; Lee and Stewart, 1981), and for evaluating the performance of a sparse regional network (Li and Thurber, 1991). Unfortunately, this method has little application in monitoring hydraulic fractures until recently. Rieven and Rodi (1995) used a method similar to that of Li and Thurber (1991) to systematically analyze location errors for earthquakes induced by hydraulic fracturing at ARCO's WDTI test site following this experiment. However, to best of our knowledge, no location error analysis has been done prior to a fracture experiment to obtain insight how the geometry effects on location accuracies. In this study, we will analyze location ambiguity and location uncertainties, in both absolute and relative senses, for a given velocity model and source-receiver configuration in an upcoming UPRC hydrofracturing experiment and provide some recommendations and suggestions in advance. Furthermore, our results suggest that the location uncertainty analysis can be developed as a practical tool for optimally designing a seismic monitoring system for imaging fractures with two monitoring wells.

PRINCIPLES OF LOCATION ERROR ANALYSIS

In a seismic event location problem, we are concerned with an inversion problem for solving the condition equations:

$$\mathbf{Ax} = \mathbf{d}, \tag{1}$$

where $\mathbf{A}$ is an m x 4 matrix of partial derivatives, $\mathbf{x}$ is a vector of four unknown hypocentral parameters, and $\mathbf{d}$ is the vector of m observed traveltime data. Elements in three of the four columns of the Jacobian matrix $\mathbf{A}$ are spatial partial derivatives of traveltimes. These derivatives can also be expressed in terms of velocity at a source point and the direction cosines of ray paths from the source to receivers (Lee and Stewart, 1981). Therefore, matrix A can be constructed easily as long as the velocity at the source and the ray paths are known.

Since earthquakes are located with a velocity model and arrival time data that contain errors, the resulting location and origin time also contain errors. Since the location and origin time are found using generalized inversion, the issue is how this operation causes errors in the data to affect the uncertainty of the solution. It is well-known that if matrix **A** is ill-conditioned, the solution of **x** will have a larger uncertainty, and if matrix **A** is well-conditioned, the solution of **x** will have a smaller location error. Therefore, matrix **A** inherently contains information about the location capability for a given source-receiver geometry. Using the singular-value decomposition (SVD) theorem (Lawson and Hanson, 1974), matrix **A** can be decomposed into:

$$\mathbf{A} = \mathbf{U}\mathbf{S}\mathbf{V}^T, \tag{2}$$

where **U** is an m x 4 matrix of an orthogonal singular vector associated with the observed data **d**, **V** is a 4 x 4 matrix of an orthogonal singular vector associated with unknown hypocentral parameters **x**, and **S** is a 4 x 4 diagonal matrix of singular values of **A**. The ratio of the largest to the smallest singular value is defined as the condition number of **A**, which is an upper bound in magnifying the traveltime errors to the location uncertainties.

Assuming variances (σ) of traveltime data are equal and independent for each observed datum, the covariance matrix **C** for the parameter space is

$$\mathbf{C} = \mathbf{V}\mathbf{S}^{-2}\mathbf{V}^T\sigma^2. \tag{3}$$

The elements of the diagonal of matrix **C** are estimates of uncertainties in the unknown hypocentral parameters. We can derive the origin time and the focal depth uncertainty as well as the epicentral error ellipse from matrix **C**, as long as the velocity model, source-receiver geometry, and traveltime data variances are known.

In earthquake location problems, a velocity model is of critical importance for calculating the ray paths and traveltimes of seismic waves passing through the ray paths. There are two major error sources for locating an earthquake: One is from an incorrect velocity model used for location, the other is the measurement error for the arrival times of seismic phases at receivers. The incorrect velocity model will bias the absolute location of an event significantly, but has less of an effect on the relative location of two or more events very close to each other (Jordan and Sverdrup, 1981, Rodi *et al.*, 1993), since the systematic error caused by an incorrect velocity model can be eliminated or reduced by using station corrections. This is the basic idea of Joint Hypocenter Determination (JHD) (Douglas, 1967). The second type of error—the reading error of arrival times—can be significantly reduced by using waveform correlation analysis (Poupinet *et al.*, 1984; Phillips *et al.*, 1992; Moriya *et al.*, 1994; Li *et al.*, 1995a,b). This kind of error mainly affects the accuracy of relative source locations among a cluster of seismic events. Therefore, we can obtain high-precision relative event locations by using both JHD idea and waveform correlation analysis.

In the practice of earthquake location, if arrival time data at multiple stations are available, we can estimate the origin times and hypocentral locations for a group of

seismic events based on traveltimes calculated with a given velocity model. The misfits between theoretical traveltimes and observed data are traveltime residuals. The traveltime residuals contain the contribution from both the velocity model errors and the reading errors of the arrival times of seismic phases. We can roughly separate the velocity model error by statistically analyzing the common part of the traveltime residuals for a cluster of seismic events at each station and then correct it with a station correction model. After the station correction is applied, the rest of the residuals are dominated by the reading errors and random errors.

The objective of this study is to assess the uncertainties of earthquake locations in both absolute and relative senses. The major purpose of the UPRC fracturing project is to estimate the fracture azimuth, length, and height. Therefore, the accuracies of relative source locations will be our major concern. For comparison, we also derived the absolute location uncertainties based on given velocity models. We will calculate the 95% confidence regions for five hypothetical seismic sources along an expected fracture zone in three different layers at the UPRC fracturing test site.

UPRC HYDROFRACTURING EXPERIMENTS AT CARTHAGE FIELD

The UPRC hydrofracturing experiment site is located at Carthage Field, Panola County, Texas. Carthage Field, discovered in 1968, is a thickly layered, low permeability gas reservoir. It is currently experiencing a fourth active drilling period with numerous wells drilled in 80-acre spacing. The major geological units in the Carthage gas field are a series of sand/shale formations. One of the most important production regions is called the Cotton Valley.

To better characterize the fractures in the Cotton Valley, UPRC carried out a pilot experiment to detect microearthquakes in the Carthage Field in May 1994, with fracture treatment at a depth of 9508 ft, and a three-component geophone in a monitor well at a depth of 9025 ft, and a three-component geophone at the surface. Eighteen seismic events induced by hydrofracturing were detectable and located by the borehole geophone at distances exceeding 1300 ft in Carthage's sand and shale formations, where the monitor well was offset significantly from the fracture plane. Following this successful pilot test, a massive hydraulic fracturing experiment was planned at Carthage Field for 1996.

A schematic of configuration for a treatment well (#21-10) and two monitor wells (#21-9 and #22-9) to be used in a massive fracture experiment in the Carthage Field is shown in Figure 1. The horizontal distances from the fracture treatment well (F01) to two monitor wells, (M01 and M02), are 1257 and 1080 ft, respectively (Figure 2). The dashed line in Figure 2 indicates an assumed azimuth of an expected hydraulic fracture zone. The expected fracture orientation is assumed along a strike of about $N70^oE$ based on geological information and downhole stress measurement. UPRC's pilot study (Zhu *et al.*, 1996) roughly estimated that the fracture has an orientation of about $N65^oE$ and

a half-length of 600 to 800 ft.

Figure 3 shows a schematic of the geophone arrays in the two monitor wells to be used for the proposed hydrofracturing project. Monitor wells M01 and M02 will be equipped with 47 and 49 three-component geophones with 50-ft spacing, respectively. 288 signal channels will be used to record seismic signals generated by the induced microearthquakes, with a sampling rate of at least 1000 samples per second. Geophones in well M01 span a depth range of 7650 to 9950 ft and the seismometers in well M02 have a depth range of 7650 to 10050 ft (Figure 3). The fracture treatments will be conducted at fracture well (F01) in three different layers: (1) Upper Cotton Valley, (2) Middle Cotton Valley, and (3) Taylor. The center of each layer is located at 8450, 9050, and 9750 ft, respectively. We refer to them as layer 1, 2 and 3, respectively, throughout this paper.

Figure 4 shows a linear gradient velocity model for P- and S-waves for the Carthage experiment site. This P-wave velocity model was developed based on the sonic well log. The S-wave velocity model was estimated using Castagna's Vp/Vs relation (Castagna, 1993). In our error analysis for seismic source locations, we will use this linear gradient velocity model to calculate ray paths, traveltimes, and partial derivatives of the seismic rays and to construct matrix **A** in equation (1). To access the spatial variation of the source location uncertainties for a given geometry of geophone arrays, we selected five hypothetical sources (events A, B, C, D, and E) along the assumed strike of the expected fracture zone (Figure 5). The five hypothetical sources are evenly distributed along the expected strike of a fracture zone with the middle event (source C) situating within the treatment well (F01). The distances between these hypothetical sources are 500 ft. In the following sections, we start with the analysis of the location ambiguity caused by two-station locations, and then calculate 95% confidence regions for the five hypothetical sources in both absolute and relative senses.

LOCATION AMBIGUITY WITH TWO VERTICAL ARRAYS

There will be only one vertical array in each of the two monitor wells in the UPRC massive fracturing experiment. Locating epicenters of induced earthquakes with two vertical arrays is equivalent to a two-station location problem. It is well-known that without azimuthal information, there is a fundamental ambiguity in the source location: two points located symmetrically about the line connecting two observing stations will always fit the arrival time data equally well (Li and Thurber, 1991). Rieven and Rodi (1995) found this kind of location ambiguity using only arrival time data from two arrays in the two monitor wells of ARCO's WDTI experiment.

Using the proposed seismic array configuration in the upcoming UPRC fracturing experiment, we calculated ambiguity locations (A', B', C', D' and E') for five hypothetical sources (A, B, C, D, and E) along the expected strike of the fracture zone at the Carthage test site. We call these ambiguity locations of hypothetical seismic sources ghost images of the real hypothetical sources. Figure 6 shows the locations of five hy-

pothetical sources and their ghost images as well as the locations of two arrays in two monitor wells (M01 and M02) used for locating the sources. The five hypothetic sources span a distance range of 2000 ft along an assumed strike of the expected fracture zone.

Figure 6 clearly shows the location ambiguity with the two vertical arrays in the two monitor wells. The effects of this ambiguity to the source locations are two-fold. First, events within the target fracture zone may be located at the locations of their ghost images, resulting in significant uncertainties in estimating the fracture length and orientation. For example, if five real hypothetical sources are all 'mistakenly' located at the locations of their ghost images, then the orientation of the fracture zone will be estimated at about $N90^oE$ rather than $N70^oE$. Second, a real seismic source situated at the region where the five ghost images are located may be mistakenly located within the fracture zone. The location ambiguity effects will be even worse if there is scattered background seismicity associated with neighboring production wells which were fractured previously, as shown by Zhu *et al.* (1996). In order to obtain reliable and accurate estimates of the fracture orientation and length, we have to remove or at least reduce such an ambiguity effect.

The simplest approach to overcome this kind of location ambiguity problem is to use three or more stations (monitor wells) at different azimuths. For example, Wills *et al.* (1992) used four arrays in three monitor wells, and House (1987), Phillips *et al.* (1992), and Li *et al.* (1995a) used four borehole stations to locate the induced microearthquakes. However, increasing the number of monitor wells will increase the cost of the experiment tremendously and may not be feasible for the planned UPRC massive hydrofracturing experiment. Adding a few stations at the surface could be possible and cheaper solution. However, a three-component geophone at the surface deployed during a pilot study at UPRC's Carthage test site observed no seismic signals from the deep hydraulic fracturing, since the fractures may be too deep to be recorded at the surface (Zhu *et al.*, 1996).

An alternative and feasible way to remove such location ambiguity is to make use of the arrival azimuth data along with the arrival time data (Li and Thurber, 1991), since azimuth data provide directional information. Li and Thurber (1991) demonstrated the importance of azimuthal data in locating earthquakes using a sparse network. For the case of two-station locations, arrival azimuths, estimated from the particle motion of P-waves at observing stations (e.g., Magotra *et al.*, 1987; Thurber *et al.*, 1989), cannot only readily remove the location ambiguity but also reduce the error ellipses of epicenter locations (Li and Thurber, 1991). Arrival azimuthal information is obviously the key to the single-station location (Bratt and Bache, 1988; Li and Thurber, 1991), since arrival time data from multiple seismic phases at a single station alone can reliably determine the distance range but provide no information on direction. However, a theoretical analysis of the single-station location problem by Li and Thurber (1991) indicated that the epicenter constraint will always be relatively weak due to the relative inaccuracy of arrival azimuth estimation (generally 5 to 10^o uncertainty). Zhu *et al.* (1996) used both the arrival time and azimuth data from a downhole, three-component

geophone to estimate epicentral locations for 18 microearthquakes recorded during the pilot fracturing experiment at the Carthage test site. Arrival time and azimuth errors are estimated to be about 16 ms and 5°, respectively, and the semimajor and semiminor axes of the error ellipses for epicenters are 400 and 150 ft, respectively.

Although arrival azimuth information will help to remove the location ambiguity from two-station locations, an accurate estimate of the arrival azimuth is not an easy task. The major technical difficulty is how to accurately determine the orientations of the horizontal geophones in deploying the geophone arrays in the deep boreholes. One approach to obtain a reliable estimate of the arrival azimuths is to make use of both calibration shots near the surface and downhole implosive sources in a crosshole survey. We recommend using calibration events along the target fracture zone and in the region where the ghost images are situated. Horizontal-component waveforms of the calibration events with known locations can be used to accurately and reliably determine the orientations of horizontal components of the downhole geophones. The secondary advantage of calibration events with known origin times is to provide information about the effects of velocity model uncertainties which can be used in a station correction model.

From Figure 6 we also note that the location ambiguity effect is different for hypothetical sources at different positions along the assumed fracture. For hypothetical events A, B, C, and D, their ghost images are significantly separated from their real locations. Therefore, adding arrival azimuthal data can immediately remove such location ambiguity. However, the hypothetical event E is too close to its ghost image. Adding azimuth information cannot easily distinguish events E and E' since the azimuth itself has the measurement error of 5° to 10°. Based on this analysis, we can conclude, without doing calculations for error ellipses, that the location uncertainties for events close to sources E and E' will be significantly larger than those for events close to the other four hypothetical sources.

VELOCITY MODEL AND TRAVELTIME RESIDUAL

To estimate source location uncertainties with the SVD method, we need traveltime data variances to calculate the location errors with equation (3). How to access the data variances for traveltimes is addressed in this section. In earthquake location practice, data variances of traveltimes due to uncertainties of a velocity model and reading errors of arrival times are typically estimated by comparing the residuals between the observed and theoretically calculated (with a given model) traveltimes at multiple observing stations. The root-mean-squared (RMS) residuals of traveltimes are typically used as indicators for the location uncertainties. For a cluster of events close to each other, the RMS residuals calculated with multiple stations can be obtained. We can obtain data variances of traveltimes by statistically analyzing the multiple-station and multiple-event RMS residual data.

Since no multiple-event and multiple-station arrival time data are available yet at

UPRC test site, we try to roughly estimate the data variance of traveltimes with some synthetic data using the configuration of geophone arrays for the upcoming UPRC fracture experiment and two simplified velocity models. To assess the data variances of traveltimes caused by velocity models, we selected five hypothetical seismic sources, events A, B, C, D and E, along the expected strike of the hydraulic fracture zone (Figure 5), and calculated and compared traveltimes of P- and S-waves to the two monitor wells for two different velocity models: A linear gradient velocity model (shown in Figure 4) and the other is a constant velocity model. In the constant velocity model, we averaged velocities for depths between 7650 and 10050 ft as the constant values for the P- and S-waves, respectively. We derived Vp = 15700 ft/s and Vs = 9700ft/s. The constant velocity model is similar to that used by Zhu *et al.* (1996) with a slightly larger (5%) velocity value since the hypothetical sources in this analysis are much deeper than that of the pilot study (Zhu *et al.*, 1996). Calculating the traveltimes for the constant velocity model is quite straightforward since we only deal with the ray path of a straight line. For the linear gradient velocity model, the curvature of the seismic ray path has to be taken into account. Refer to Lee and Stewart (1981) for more details about calculating traveltimes along curved ray paths.

Figure 7 plots the traveltime time differences between the two velocity models as a function of receiver depths with the hypothetical source (C1) at the treatment well (F01) in the layer of Upper Cotton Valley. The maximum traveltime differences are observed to be about 3 and 5 ms for P- and S-waves, respectively, at both monitor wells. Figure 8 shows traveltime differences of P- and S-waves for the two different velocity models at two monitor wells with a hypothetic seismic source (A3) at the layer of Taylor. The traveltime differences are about 5 and 8.7 ms for P- and S-waves, respectively. We note that the traveltime differences are substantially increased as a result of increasing hypocentral distances to the two monitor wells.

Table 1 summarizes the maximum traveltime differences between a linear gradient velocity model and a constant velocity model for five hypothetical sources (A, B, C, D, and E) in three different layers (1 = Upper Cotton Valley, 2 = Middle Cotton Valley, and 3 = Taylor). The minimum and maximum time differences between the two models are 1.5 and 5.3 ms for P-waves. The S-wave traveltime residuals between the two models range from 2.4 to 8.6 ms. For all five hypothetical sources at three different layers, it is shown that the traveltime residuals between the two models increase as the epicentral distances increase. For each hypothetical source, the traveltime residuals between the two models are smallest for the sources at layer 2 for both P- and S-waves with only a few exceptions (Table 1).

Using the traveltime residuals between the two velocity models for each hypothetical source at 96 geophones, we calculate the RMS and maximum traveltime residuals for the five hypothetical sources in three different layers. The maximum and RMS S-wave traveltime residuals are plotted in Figure 9. For both RMS and maximum traveltime residuals of the S-wave, the residuals are largest for event A and smallest for event E. The RMS residuals range from 1.5 to 4.5 ms with an average RMS residual of 2.4 ms for

Table 1: Average Traveltime Residuals at Each Station

Source Location	M01 P (ms)	S(ms)	M02 P(ms)	S(ms)
A1	4.55	7.37	4.11	6.66
A2	3.94	6.38	3.25	5.27
A3	5.34	8.56	4.50	7.29
B1	3.72	6.11	3.28	5.32
B2	3.24	5.25	2.61	4.23
B3	4.21	6.92	3.40	5.51
C1	2.96	4.80	2.56	4.15
C2	2.64	4.27	2.14	3.46
C3	3.15	5.11	2.39	3.81
D1	2.38	3.85	2.07	3.35
D2	2.19	3.55	1.92	3.12
D3	2.28	3.69	1.61	2.60
E1	2.12	3.43	1.99	3.23
E2	2.00	3.24	1.89	3.07
E3	1.86	3.01	1.47	2.38

the 15 hypothetical sources. The maximum residuals are 3.0 to 8.7 ms with an average value of 5 ms. Figure 9 also shows typical traveltime errors derived from the pilot study with data from a single three-component geophone and 18 microearthquakes (Zhu *et al.*, 1996).

Li *et al.* (1995a) found an average absolute RMS residual of 4 to 5 ms for 157 induced microearthquakes in a hard formation in Fenton Hill, New Mexico. Rieven and Rodi (1995) obtained an average RMS residual of 6 ms for induced earthquakes in a soft formation in Jasper, Texas. The average RMS value we estimated for the UPRC test site with the simplified velocity models is smaller by factors of 2 to 3 than those obtained from the other location practices for induced earthquakes. However, our average maximum residual is comparable to these typical RMS residuals from other location practices. Therefore, we believe that our RMS estimates may underestimate the real traveltime residuals due to our two velocity models being significantly simplied. Our maximum residuals may better represent the typical errors of traveltimes. Zhu *et al.* (1996) obtained a typical traveltime error of about 16 ms. We believe that this value may represent a maximum bound of the traveltime errors.

Based upon the analysis of traveltime residuals for synthetic and real data at the UPRC fracturing test site, we specified two standard deviation models: (1) constant σ and (2) variable σ models. In the constant σ model, we assume $\sigma = 10$ ms for all events along the expected fracture zone. This is a conservative estimation since the value is about two times larger than the average maximum traveltime residual we derived using synthetic data. If we take into account the effects from the lateral heterogeneity of

the real earth structure, sharp interfaces and anisotropy in the propagation medium, the large standard deviation value in the constant model is even more reasonable. This model provides an upper bound of estimates for absolute uncertainties in the traveltimes. The variable σ model takes the spatial variation (Figure 9) of traveltime residuals into account. In the variable σ model, we use the S-wave maximum traveltime residuals for five hypothetical sources in layer 2 (Table 1 and Figure 9) as the standard deviation for each corresponding hypothetical source. This model provides a lower bound of estimates for absolute uncertainties in the traveltimes.

ABSOLUTE SOURCE LOCATION UNCERTAINTIES

So far, we have discussed the basic principle for estimating source location uncertainties in both absolute and relative senses using the SVD method. In this section, we estimate the absolute location uncertainties for hypothetical microearthquake sources in UPRC's hydrofracturing test site at Carthage Field, Panola, Texas, using a linear gradient velocity model (Figure 4) and 96 three-component geophones of two arrays that will be deployed into two monitor wells (Figure 3).

To estimate the uncertainties of source locations, we need to compute the ray paths, traveltimes between a source and a set of geophone arrays along the ray paths, and the corresponding spatial derivatives evaluated at the source using a given velocity model and the geometry configuration of geophone arrays. For a linear gradient velocity model, we deal with the curvatured ray paths from a source to the geophone receivers. The direction cosines of the seismic rays are the cosines of the direction angles which are defined with respect to the positive direction of the coordinate axes. The spatial derivatives of the traveltimes can be expressed in terms of the velocity at the source point and the direction cosines of the ray paths from the source to the receivers. Therefore, it is easy to construct matrix **A** in equation (1), using direction cosines of the seismic rays and the velocity at the source. With an SVD method (equation 2) and standard deviation models as variances of traveltime data, we will construct the covariance matrix (equation 3) and estimate the source location uncertainties, including the epicentral error ellipse and depth uncertainty.

Location Uncertainties: Constant Vs. Variable σ Models

First, we calculated the absolute location error ellipsoids (95% confidence regions) for the five hypothetical sources and their ghost images in layer 2 (Middle Cotton Valley) using the constant σ model (σ = 10 ms). Figure 10 is a map view showing error ellipses for these hypothetical sources and their ghost images at layer 2. A striking feature of Figure 10 is the extremely large error ellipses for the hypothetical source E and its ghost image E', as we expected previously from the analysis of the location ambiguity. The strike of the semimajor axis of the error ellipse ranges from $N71°E$ to $N80°E$ for hypothetical sources from E to A. For their ghost images E' to A', the strike of the semimajor axis of the error ellipse is from $N79°E$ to $N87°E$. The semimajor axis (a) of the error ellipse

increases when the hypothetical source moves from A to E. The semimajor axes of error ellipses at sources A and E are about 80 ft and 580 ft, respectively. Significant variation of the semimajor axis will occur for events close to the hypothetical source E. From source A to E, the semiminor axis decreases from 57 to 23 ft. Since a constant σ model is used, the significant spatial variation of the epicenter error ellipses (Figure 10) can only be attributed to the station-receiver configuration geometry, which significantly amplifies the traveltime errors to the location uncertainties. We believe that the absolute location uncertainties derived based on the constant σ model represent an upper bound of estimates for absolute location errors.

Second, we calculated the absolute location uncertainties (95% confidence regions) for the five hypothetical sources and their ghost images in layer 2 (Middle Cotton Valley) with the variable σ model (σ = 3.5 to 6.5 ms). Figure 11 plots the epicenter error ellipses for the hypothetical sources A to E and their ghost images A' to E'. The semimajor axis (a) for source A to E varies from 39 to 212 ft. The semiminor axis (b) for sources A to E decreases from 37 ft to 8 ft. As one can see from Figure 11, the semimajor axes of the error ellipses for sources A to E, especially for source E, are significantly reduced compared to the results from the constant σ model (Figure 10). We attribute this significant improvement to a fact that the spatial variation of the traveltime residuals have been taken into account. However, the semimajor axis (a) of the error ellipse for the source E is still quite large. The absolute location errors derived from the variable σ model can be assumed as a lower bound of estimates for the absolute location uncertainty.

The depth uncertainties of five hypothetical sources in layer 2 (Middle Cotton Valley) are calculated with both constant and variable σ models and are compared in Figure 12. The depth uncertainties estimated with both σ models show the same trend: the depth uncertainty increases as the epicentral distance between the source and geophone arrays increases (from source E to A). For the constant σ model, the depth uncertainty ranges from 27.4 to 55.2 ft. The depth uncertainty estimated with the variable σ model varies from 9.4 ft at source E and 35.3 ft at source A.

Figure 13 shows the semiminor axes (b) of epicenter error ellipses calculated with both constant and variable σ models for the five hypothetical sources at layer 2. From source A to E, the semiminor axes estimated with both models monotonously decrease as the epicentral distances decrease. The smallest and largest semiminor axis obtained with the constant σ model are 22.5 ft at source E and 57.3 ft at source A, respectively. The minimum and maximum semiminor axes are estimated to be 7.7 and 36.7 ft, respectively, using the variable σ model. From Figures 12 and 13, we find that both depth uncertainties and semiminor axes (b) derived with a variable σ model are smaller than those estimated using the constant σ model by factors of 1.5 to 3 for the five hypothetical sources, from A to E.

Using both constant and variable σ models, we also calculated and compared the semimajor axes (a) of epicentral error ellipses for five hypothetical sources at layer 2. The spatial variation trend of the semimajor axes (Figure 14) are different from those of

the depth uncertainty and the semiminor axis (Figures 12 and 13). For the constant σ model, the semimajor axis increases as the epicentral distances between the source and receivers decrease (form source A to E). The semimajor axis of the epicenter error ellipse dramatically jumps to 619.2 ft at the hypothetical source E. The large semimajor axis at source E is about 5 times larger than at source D (129.9 ft) and 8 times larger than at source A (80.1 ft). This indicates that the source-receiver geometry configuration significantly amplifies the traveltime errors to the location uncertainties, especially for the semimajor axis of the epicentral error ellipse, for events close to the hypothetical source E. The spatial variation pattern for the semimajor axis of the error ellipse derived with the variable σ model differs slightly from that estimated with the constant σ model. ¿From Figure 14 one can see that the semimajor axis is smallest (39.1 ft) at source C (within the fracture well F01). At sources A, B, and D, the semimajor axes increase to 51.3, 43.9, and 46.1 ft, respectively. The semimajor axis at source E is still the largest (211.8 ft), but it is about three times smaller than that estimated with the constant σ model (Figure 14).

The ratio of the semimajor axis and semiminor axis (a/b) and the area of the epicenter error ellipse (πab) for the five hypothetical sources at layer 2 are also calculated with both the constant and variable σ models and plotted in Figures 15 and 16, respectively. The a/b ratio curve (Figure 15) is identical for both σ models, indicating that the a/b ratio is mainly controlled by the geometry configuration of the source-receiver arrays rather than by traveltime errors caused by velocity models. The a/b ratio increase from 1.4 at source A to 5.1 at source D. The largest a/b ratio is 27.5 at source E. Figure 16 indicates that the error ellipse areas calculated with the variable σ model are significantly smaller than those estimated with the constant σ model, especially at source E. It also shows that the error regions are relatively small for seismic events occurring between sources B and D. When events occur somewhere between D and E, the source location uncertainties will significantly increase.

Location Uncertainties: Spatial Variation

We have analyzed the location uncertainties for five hypothetical sources at the same depth (layer 2), distributing along the assumed strike of an expected fracture zone, with two models for standard deviations. Now we examine the spatial variation of the absolute location uncertainties for five hypothetical sources at three different layers using the constant σ model. We calculated the epicentral error ellipse (orientation, semimajor axis, a, and semiminor axis, b), the depth uncertainty, dz, and the semimajor axis of the hypocenter error ellipsoid, dr, and the error in the origin time estimate, dt, for five hypothetical sources (A, B, C, D, and E) and their ghost images (A', B', C', D', and E'). The results are summarized in Table 2.

Figure 17 shows the epicenter error ellipses for three hypothetical sources (B, C, D) in three different layers (1, 2, and 3). For each of the three sources, the strike of the error ellipse changes little when the source depths vary. The maximum azimuth variation of the ellipse strike for each source at three different depths is less than 1.4°. For each of

Table 2: Absolute Source Location Uncertainties ($\sigma = 10ms$)

Source Location	Strike (N^oE)	a (ft)	b (ft)	dz (ft)	dr (ft)	dt (ms)
A1	70.8	77.8	56.8	55.3	111.1	6.17
A2	71.1	80.1	57.3	55.2	112.9	6.16
A3	73.8	81.3	61.8	65.1	121.1	6.20
B1	71.1	81.0	45.2	46.0	103.5	6.04
B2	71.2	83.6	45.5	45.0	105.2	6.02
B3	72.5	83.4	50.1	57.8	113.2	6.14
C1	72.2	88.7	34.3	37.9	102.4	5.72
C2	72.2	91.5	34.5	36.1	104.2	5.66
C3	72.7	90.5	39.0	53.1	111.9	6.01
D1	75.4	126.8	25.4	31.7	133.2	5.07
D2	75.4	129.9	25.6	29.5	135.7	4.96
D3	75.3	131.3	29.5	50.8	143.8	5.78
E1	80.0	606.7	22.3	29.7	607.8	4.76
E2	80.0	619.2	22.5	27.4	620.2	4.62
E3	80.0	638.1	25.9	50.0	640.6	5.67
A'1	87.0	77.9	56.4	55.2	110.9	6.17
A'2	86.7	80.2	56.8	55.1	112.7	6.16
A'3	84.4	81.3	61.3	65.0	120.8	6.20
B'1	86.8	81.1	44.8	45.9	103.4	6.04
B'2	86.7	83.7	45.1	44.9	105.2	6.02
B'3	85.6	83.6	49.7	57.7	113.1	6.14
C'1	86.0	89.0	34.1	37.9	102.6	5.72
C'2	86.0	91.8	34.3	36.1	104.4	5.66
C'3	85.5	90.8	38.7	53.1	112.1	6.01
D'1	83.4	128.0	25.3	31.7	124.3	5.07
D'2	83.4	131.2	25.5	29.5	136.8	4.96
D'3	83.4	132.6	29.4	50.8	145.0	5.79
E'1	79.2	564.7	22.3	29.7	565.9	4.76
E'2	79.2	576.3	22.5	27.4	577.4	4.62
E'3	79.2	593.9	26.0	50.0	596.5	5.67

the three sources, the semimajor and semiminor axes of the ellipse are smallest in layer 1. The semimajor and semiminor axes of the ellipse increase when the source depths increase. However, the maximum variation in the semimajor and semiminor axes due to a change in source depths are less than 5 ft. Thus, we conclude that the variation of location uncertainties for these hypothetical sources is not significant when the source depth varies from 8450 to 9750 ft.

The semimajor axes, a, of the error ellipses for five hypothetical sources at three different depths are plotted in Figure 18. For each of the five sources, the semimajor axis is smallest when the sources are in the first layer (Upper Cotton Valley). If the hypothetical sources are in layers 2 and 3, the semimajor axes of the error ellipses are slightly larger than those for the sources at layer 1. But the relative variation of the semimajor axes due to changes in the source depths is less than 5%. For hypothetical sources A, B, C, and D, the semimajor axes of error ellipses vary from 78 to 131 ft. The semimajor axis of the error ellipse for hypothetical source E jumps to a range of 606 to 638 ft. This is the largest value for the semimajor axis of the epicenter error ellipse and represents the maximum location error for the epicenter if our constant σ model is reasonable.

Figure 19 shows the semiminor axes of the epicenter error ellipses for five hypothetical sources in three different layers. For each of the five hypothetical sources, the semiminor axis is the largest when the sources are in layer 3 (Taylor). The semiminor axes of the error ellipses for each of the five sources at layers 1 and 2 are very similar to each other. The relative variation of the semiminor axes due to variation of the source depths ranges from 9% to 16%. It is shown that the semimajor axis of the error ellipse gradually decreases, from source A to E, when the distances between the sources and the geophone arrays decrease. The largest and smallest semimajor axes of the absolute error ellipses are 62 ft (at source A3) and 22 ft (at source E1).

Depth uncertainties for the five hypothetical sources at three layers are shown in Figure 20. The depth uncertainty for each of the five sources is the largest when the sources are in layer 3 (Taylor). The major feature in the depth uncertainty plot (Figure 20) is that the variation of depth uncertainties caused by changing the depths of the five hypothetical sources is significant. The relative variation of the depth uncertainties due to change of the source depths ranges from 15% (at source A) to 45% (at source E). It is also true that the depth uncertainties for five sources at three layers decrease when the distances between the sources to the geophone arrays decrease. The maximum and minimum of the absolute depth uncertainties are 65 ft (at source A3) and 27 ft (at source E), respectively.

RELATIVE LOCATION ERRORS

Calculating the relative source location uncertainties is relatively easier than calculating the absolute location uncertainty because the velocity model error has been removed or at least reduced by a station correction model. Therefore, the reading error of arrival

times will be a major contributor to the relative source location error. It has been proven that the waveform correlation analysis (Poupinet *et al.*, 1984; Ito, 1985; Fremont and Malone, 1987; Phillips *et al.*, 1992; Deichmann and Garcia-Fernandez, 1992; Moriya *et al.*, 1994; Li *et al.*, 1995b, 1996) using a master-slave event pair can significantly improve accuracies for arrival time picks. The differential arrival times can be picked to an accuracy of one sample interval or even better (Poupinet *et al.*, 1984; Deichmann and Garcia-Fernandez, 1992; Li *et al.*, 1995b). Therefore, we can approximate the reading accuracy of the arrival times as the data variance for traveltimes in a relative sense.

In a hydrofracturing experiment in Los Alamos, the sampling rate was 5000 samples per second (House, 1987; Phillips *et al.*, 1992; Li *et al.*, 1995a, 1996). In UPRC's pilot study (Zhu *et al.*, 1996) and in ARCO's WDTI experiment (Atlantic Richfield Corporation, 1994; Rieven and Rodi, 1995), 0.5 ms was used as the sampling interval. These values help us to specify the standard deviation for variances of traveltime data in a relative sense. For a conservative estimate, we selected a constant model with $\sigma =$ 1 ms as the data variance of traveltimes for estimating relative location uncertainties.

We calculated the relative source location uncertainties with the standard deviation of $\sigma = 1$ ms. The relative location uncertainties are calculated for the five hypothetical sources (A, B, C, D, and E) and their ghost images (A', B', C', D', and E'). The parameters describing the relative source location uncertainties include the epicenter error ellipse (strike, semimajor axis, and semiminor axis), the depth uncertainty, and the semimajor axis of the hypocenter error ellipsoid, and the error in the estimate of origin time. These parameters are listed in Table 3.

We compared the absolute and relative error ellipses of epicenters for three hypothetical sources (C, B, and D) at layer 2 (Middle Cotton Valley) shown in Figures 21, 22, and 23. The relative error ellipses are significantly smaller than those of the absolute error ellipses by factors of 10. For the hypothetical source C2, the semimajor and semiminor axes of the error ellipse are 9.2 and 3.4 ft in the relative sense and 91.5 and 34.5 ft in the absolute sense. The area of the relative error ellipse for source C2 (Figure 21) is smaller than the absolute error ellipse by factors of 100. The areas of the relative error ellipses are 98.2, 106.2, 121.4 square-feet for hypothetical sources C, D, and B, respectively. The area is smallest for the source at C and then increases as the source moves to B and D. The a/b ratios of sources B, C, and D are 1.8, 2.7, and 5.0, indicating that the error ellipse is significantly elongated from source B to D (Figures 21 to 23). These numbers clearly reflect that the spatial variations are not the same for the different location uncertainty parameters.

The different spatial variations for the semimajor and semiminor axes of the epicenter error ellipses and the depth uncertainty are further shown in Figures 24 to 26. As the hypothetical source moves from A to E, the semimajor axis (Figure 24) increases but the semiminor axis (Figure 25) and the depth uncertainty (Figure 26) decrease. The semimajor axis of the relative error ellipse varies from 7.8 to 13.1 ft form source A to D, and then suddenly jumps to about 64 ft at source E. This is the largest relative location error for the five hypothetical sources at three different depths. The semiminor axis of

Table 3: Relative Source Location Uncertainties ($\sigma = 1ms$)

Source Location	Strike (N^oE)	a (ft)	b (ft)	dz (ft)	dr (ft)	dt (ms)
A1	70.8	7.8	5.7	5.5	11.1	0.62
A2	71.1	8.0	5.7	5.5	11.3	0.62
A3	73.8	8.1	6.2	6.5	12.1	0.62
B1	71.1	8.1	4.5	4.6	10.4	0.60
B2	71.2	8.4	4.6	4.5	10.5	0.60
B3	72.5	8.3	5.0	5.8	11.3	0.61
C1	72.2	8.9	3.4	3.8	10.2	0.57
C2	72.2	9.2	3.4	3.6	10.4	0.57
C3	72.7	9.0	3.9	5.3	11.2	0.60
D1	75.4	12.7	2.5	3.2	13.3	0.51
D2	75.4	13.0	2.6	3.0	13.6	0.50
D3	75.3	13.1	3.0	5.1	14.4	0.58
E1	80.0	60.7	2.2	3.0	60.8	0.48
E2	80.0	61.9	2.2	2.7	62.0	0.46
E3	80.0	63.8	2.6	5.0	64.1	0.57
A'1	87.0	7.8	5.6	5.5	11.1	0.62
A'2	86.7	8.0	5.7	5.5	11.3	0.62
A'3	84.4	8.1	6.1	6.5	12.1	0.62
B'1	86.8	8.1	4.5	4.6	10.3	0.60
B'2	86.7	8.4	4.5	4.5	10.5	0.60
B'3	85.6	8.4	5.0	5.8	11.3	0.61
C'1	86.0	8.9	3.4	3.8	10.3	0.57
C'2	86.0	9.2	3.4	3.6	10.4	0.57
C'3	85.5	9.1	3.9	5.3	11.2	0.60
D'1	83.4	12.8	2.5	3.2	12.4	0.51
D'2	83.4	13.1	2.5	3.0	13.7	0.50
D'3	83.4	13.3	2.9	5.1	14.5	0.58
E'1	79.2	56.5	2.2	3.0	56.6	0.48
E'2	79.2	57.6	2.2	2.7	57.7	0.46
E'3	79.2	59.4	2.6	5.0	59.7	0.57

the relative error ellipse ranges from 2.2 ft at source E to 6.2 ft at source A. The depth uncertainty in the relative sense is smallest at source E (2.7 ft) and largest at source A (6.5 ft). The spatial of variation of the relative depth uncertainty is more significant than that for the relative error ellipse of the epicenters.

We have compared the relative and absolute location uncertainties based on constant σ models with absolute $\sigma = 10$ ms and relative $\sigma = 1$ ms. If we compare the relative location errors with the absolute location uncertainties estimated using the variable σ model, we still find that the relative location uncertainty parameters, such as the semimajor and semiminor axis of error ellipses and the depth uncertainty, are smaller than those for the absolute locations by factors of 3 to 7. The relative location uncertainties are significantly reduced compared to the absolute location uncertainties for both cases.

DISCUSSION

In this study, we have used two simplified velocity models and the geometry configuration of geophone arrays of the upcoming UPRC fracture experiment to obtain synthetic traveltime data and to examine the data variances of traveltimes. Using an SVD method and the data variance models, the absolute and relative location uncertainties are estimated for five hypothetical sources at three different layers with depths ranging from 8450 to 9750 ft. The five sources are evenly distributed along an assumed strike of an expected fracture zone from southwest to northeast (from A to E) with spacing of 500 ft. Source C is situated in the center within the fracture treatment well.

The spatial variations of the location uncertainties are clearly shown by our analyses. Both the relative depth uncertainties and the relative semiminor axes of the epicenter error ellipse decrease from source A to E. The average depth uncertainty (relative) and the average semimajor axis (relative) for the five hypothetical sources in the three layers are 4.5 ± 1.2 ft and 3.9 ± 1.4 ft, respectively. However, the relative semimajor axes of the epicenter error ellipses increase from 7.8 ft at source A to 63.8 ft at source E. The semimajor axis of the error ellipse for source E is larger than the depth uncertainty and the semiminor axis by factors of 13 to 25. We attribute the very large semimajor axis of the error ellipse for source E to the fact that it is close to the line connecting the observed arrays in the two monitor wells, M01 and M02. The ill-conditioned matrix A in equation (1) results in significantly amplifying the traveltime error to the semimajor axis of the epicenter error ellipse for source E. Therefore, one can not obtain accurate epicenter estimates for events close to source E, although the source is the closest to the two monitor wells. The average semimajor axis of the epicenter error ellipse for source A to D is 9.6 ± 2.1 ft. In summary, our estimates of the relative source location uncertainties for sources A to D are 12 ft for the semimajor axis, 5 ft for the semiminor axis, and 6 ft for the depth uncertainties. The absolute location uncertainties for corresponding sources are about 3 to 10 times larger than the relative location uncertainties.

Note that the absolute location uncertainties were conservatively estimated using the two simplified velocity models and should represent the upper bound of uncertainty

estimates only when the simplified velocity models approximate the real earth structure. If the real earth structure significantly differs from what we have used due to significant lateral heterogeneity, a sharp jump of velocities at interfaces, and medium anisotropy, the absolute source location uncertainties are expected to be much larger. In the case of relative source locations, the systematic error caused by a velocity model can be removed; the measurement accuracy for arrival times is the key factor for deriving the uncertainties of relative source locations. The waveform correlation analysis can achieve a reading accuracy that is equal to or better than the sampling interval for unaliasing waveform data. In our analysis, we conservatively take σ as 1 ms. If the σ is 0.5 ms, the relative location error will be reduced by factors of 2. We strongly recommend using a sampling interval of 0.5 ms or even shorter. Selecting a better sampling rate will not only reduce the relative location uncertainty but also avoid undersampling the seismic signals. Previous spectral analysis of microearthquakes induced by hydrofracturing (Fehler and Phillips, 1991; Li *et al.*, 1995c) indicated that the corner frequencies of these induced events could be as high as 400 to 500 Hz, which is very close to the Nyquist frequency for a sampling interval of 1 ms. Note also that our analysis was done under an ideal case in which it is assumed that the hypothetical seismic events are recorded well by all geophones and all data can be used in estimating location uncertainties. In a real case, it is rear that data from all the geophones can be used in locating seismic sources. Therefore, locating events without data from all geophones may result in slightly larger location uncertainties compared to what we have estimated.

The major purpose of the UPRC hydrofracturing experiment is to accurately image the hydraulic fracture and estimate its orientation, length, and height. We have derived the location uncertainties for the hypothetical sources along the assumed strike of the expected fracture zone. We found that the strike of the epicenter error ellipse is roughly parallel to the strike of the fracture zone. Therefore, the semimajor axes of error ellipses for the sources situating at different parts of the fracture zone can be used to calculate the relative measurement error for the fracture length. Between two sources C and B in the Middle Cotton Valley, the real distance between them is 500 ft. The semimajor axes of the absolute error ellipses for the two sources are $\pm$ 91.5 ft and $\pm$ 83.6 ft, respectively. The resulting relative measurement error for the fracture length is about 35%. If the semimajor axes of the relative error ellipses are used, one can obtain the relative measurement error for the fracture length to be 4%. Figure 27 shows the relative measurement errors for sources distributed along the fracture zone using three different data variance models. The relative measurement errors are about 4% to 15% with the relative location results, but are 25% to 150% when the absolute location results are used. Although the error is smaller for source A, the longest distances between the source and two monitor wells may cause a poor signal-to-noise ratio, especially for smaller events, resulting in poor location results. Similarly, we can estimate the relative measurement error of the fracture height.

In this study, we theoretically predict the absolute and relative location uncertainties for the given velocity models, the geometry of the fracture and monitor wells, and

the geophone array configuration in the monitor wells. The analysis of the location uncertainties provides some ideas about how accurately the fracture azimuth, length, and height can be estimated in locating microearthquakes induced by hydraulic fracturing. We have found that relative source locations can significantly reduce relative measurement error for fracture length, azimuth, and height. We have also realized significant spatial variations of the absolute and relative location uncertainties. These results lead us to believe that our location uncertainty analysis should be generalized as a practical tool for optimally designing a two-well seismic monitoring system to accurately image subsurface hydraulic fractures. For the given velocity models, the geometry of the fracture, and the geophone array configuration in the monitor wells, we can search for the optimal positions for two monitor wells so that the location uncertainties (especially the depth uncertainty or one of the error ellipse axes) of sources along the fracture are minimized. Alternatively, for the given velocity models, the geometry of the fracture, and the positions of two monitor wells, one can determine how many geophones in a monitor well are necessary to achieve required location accuracies. Accomplishing this approach successfully will significantly contribute to accurate, efficient, and economic imaging of subsurface fractures.

CONCLUSIONS

We have theoretically predicted the relative and absolute location uncertainties (95% confidence regions) for hypothetical sources at three different depths along an assumed strike of a target fracture zone with given velocity models, the configuration of 96 three-component geophones in the boreholes, and the locations of two monitor wells. The assumed strike of the expected fracture zone was $N70^{o}E$. The five hypothetical sources are evenly distributed along the fracture zone and span a distance range of 2000 ft with spacing of 500 ft. The vertical extent of the hypothetical sources ranges from 8450 to 9750 ft. We determined that the typical relative location uncertainties for the five hypothetical sources at three different layers are 12 ft for the semimajor axis, 5 ft for the semiminor axis, and 6 ft for depth uncertainty. It is shown that the relative location uncertainties are significantly smaller than those of the absolute location by factors of 3 to 10. The relative measurement error for the fracture length is about 4% to 15% when the relative source location results are used. The location ambiguity from the two-station locations is discussed and the arrival azimuth data are recommended for removing such location ambiguity. We expect that our approach of the location uncertainty analysis can be generalized as a practical tool in optimally designing of a two-well seismic monitor system for high-precision imaging of subsurface fractures.

ACKNOWLEDGMENTS

We would like to thank Dr. Roger Turpening for helpful discussions. This research was supported by the Reservoir Delineation Consortium at ERL and by DOE Contract #DE-FG02-86ER13636.

REFERENCES

Atlantic Richfield Corporation, 1994. The deep well treatment and injection program, fracture technology filed demonstrate project, *Final Report,* The Atlantic Richfield Corporation, Plano, Texas, 84 pp.

Block, L.V., C.H. Cheng, M.C. Fehler, and W.S. Phillips, 1993. Seismic imaging using microearthquakes induced by hydraulic fracturing, *Geophysics, 59,* 102–112.

Bratt, S.R., and T.C. Bache, 1988. Locating events with a sparse network of regional arrays, *Bull. Seism. Soc. Am., 78,* 780–798.

Castagna, J.P., 1993. Petrophysical imaging using AVO, *The Leading Edge, 12,* 172–178.

Deichmann, N. and M. Garcia-Fernandez, 1992. Rupture geometry form high-precise relative hypocenter locations of microearthquake clusters, *Geophys. J. Int., 110,* 501–517.

Douglas, A., 1967. Joint epicenter determination, *Nature, 215,* 47–48.

Fehler, M., L. House and H. Kaieda, 1987, Determining planes along which earthquakes occur: method and application to earthquakes accompanying hydraulic fracturing, *J. Geophys. Res., 92,* 9407–9414.

Fehler, M. and W.S. Phillips, 1991. Simultaneous inversion for Q and source parameters of microearthquakes accompanying hydraulic fracturing in granitic rock, *Bull. Seism. Soc. Am., 81,* 553–575.

Fremont, M.J. and S.D. Malone, 1987. High precision relative locations of earthquakes at Mount St. Helens, Washington, *J. Geophys. Res., 92,* 10223–1023.

House, L., 1987. Locating microearthquakes induced by hydraulic fracturing in crystalline rock, *Geophys. Res. Lett., 14,* 919–921.

Ito, A., 1985. High resolution relative hypocenters of similar earthquakes by cross-spectral analysis method, *J. Phys. Earth, 33,* 279–294.

Jordan, T.H., and K.A. Sverdrup, 1981. Teleseismic location techniques and their application to earthquake clusters in south-central Pacific, *Bull. Seism. Soc. Am., 71,* 1105–1130.

Kijko, A., 1977. An algorithm for the optimum distribution of a regional seismic network, *Pure Appl. Geophys. 115,* 999–1021.

Lawson, C.L., and R.J., Hanson, 1974. *Solving Least Squares Problems,* Prentice Hall, Inc. 340 pp.

Lee, W.H.K., and S.W. Stewart, 1981. Principles and applications of microearthquake networks, *Adv. Geophys. Suppl. 2,* 293 pp.

Li, Y. and C.H. Thurber, 1991. Hypocenter constraint with regional seismic data: a theoretical analysis for the Natural Resources Defense Council Network in Kazakhstan, USSR, *J. Geophys. Res., 96,* 10159–10176.

Li, Y., C.H. Cheng, and M.N. Toksöz, 1995a. Hydraulic fracture imaging from the Los Alamos hot dry rock experiment, *Proceedings of SEG International Explosion and 65th Annual Meeting,* Huston, Texas, 223–226.

Li, Y., C. Doll, and M.N. Toksöz, 1995b. Source characterization and fault plane deter-

minations for Mblg = 1.2 to 4.4 earthquakes in the Charlevoix seismic zone, Quebec, Canada, *Bull. Seism. Soc. Am., 85,* 1604–1621.

Li, Y., C.H. Cheng, and M.N. Toksöz, 1995c. Source characterization of microearthquakes induced by hydraulic fracturing with empirical Green's function, *Annual Report,* Borehole Acoustics and Logging and Reservoir Delineation Consortia, MIT, Cambridge, Massachusetts, 7.1-7.26.

Li, Y., C.H. Cheng, and M.N. Toksöz, 1996. Seismic imaging geometry and growth process of a hydraulic fracture zone at Fenton Hill, New Mexico, Submitted to *Geophysics.*

Magotra, N., N. Ahmed, and E. Chael, 1981. Seismic event detection and source location using single station (three-component) data, *Bull. Seism. Soc. Am., 77,* 958–971.

Moriya, H., K., Nagano, and H. Niitsuma, 1994. Precise source location of AE doublets by spectral matrix analysis of triaxial hodogram, *Geophysics, 59,* 36–45.

Phillips, W. S., L. S. House, and M. C. Fehler, 1992. Vp/Vs and the structure of microearthquake clusters, *Seismol. Res. Lett., 63,* 56–57.

Poupinet, G., W. L., Ellsworth, and J. Frechet, 1984. Monitoring velocity variations in the crust using earthquake doublets: An application to the Calaversa fault, California, *J. Geophys. Res., 89,* 5719–5731.

Rieven, S. and W. Rodi, 1995. Analysis of microseismic location accuracy for hydraulic fracturing at the DWTI site, Jasper, Texas, *Annual Report,* Borehole Acoustics and Logging and Reservoir Delineation Consortia, MIT, Cambridge, Massachusetts, 5.1–7.28.

Rodi, W., Y. Li, and C.H. Cheng, 1993. Location of microearthquakes induced by hydraulic fracturing, *Annual Report,* Borehole Acoustics and Logging Consortium, MIT, Cambridge, Massachusetts, 369–410.

Thurber, C.H., H. Given, and J. Berger, 1989. Regional seismic event location with a sparse network: Application to eastern Kazakhstan, USSR, *J. Geophys. Res., 94,* 17767–17780.

Truby, L. S., R.G., Keck, and R.J. Withers, 1994. Data gathering for a comprehensive field fracturing diagnostics project: A case study. *SPE/IADC Paper 27516,* presented at the SPE/IADC Drilling Conference, Dallas, Texas, February 18–20.

Uhrhammer, R. A., 1980. Analysis of small seismographic station network, *Bull. Seism. Soc. Am., 70,* 1369–1379.

Vinegar, H., P. Wills, D. DeMartini, J., Shlyapobersky, W. Deeg, R. Adair, J. Woerpel, J. Fix, and G. Sorrells, 1992. Active and passive imaging of a hydraulic fracture in diatomite, *J. Petrol. Tech., 44,* 28–34, 88–90.

Wills, P.B., D.C., DeMartini, H.J., Vinegar, J., Shlyapobersky, W.F., Deeg, J.C., Woerpel, J.E., Fix, G.G., Sorrells, and R.G., Adair, 1992. Active and passive imaging of hydraulic fractures, *The Leading Edge, 11,* 15–22.

Zhu, X., J. Gibson, N. Ravindran, R. Zinno, D. Sixta, 1996. Seismic imaging of hydraulic fractures in Carthage tight sands: A pilot study, *The Leading Edge, 15,* 218–224.

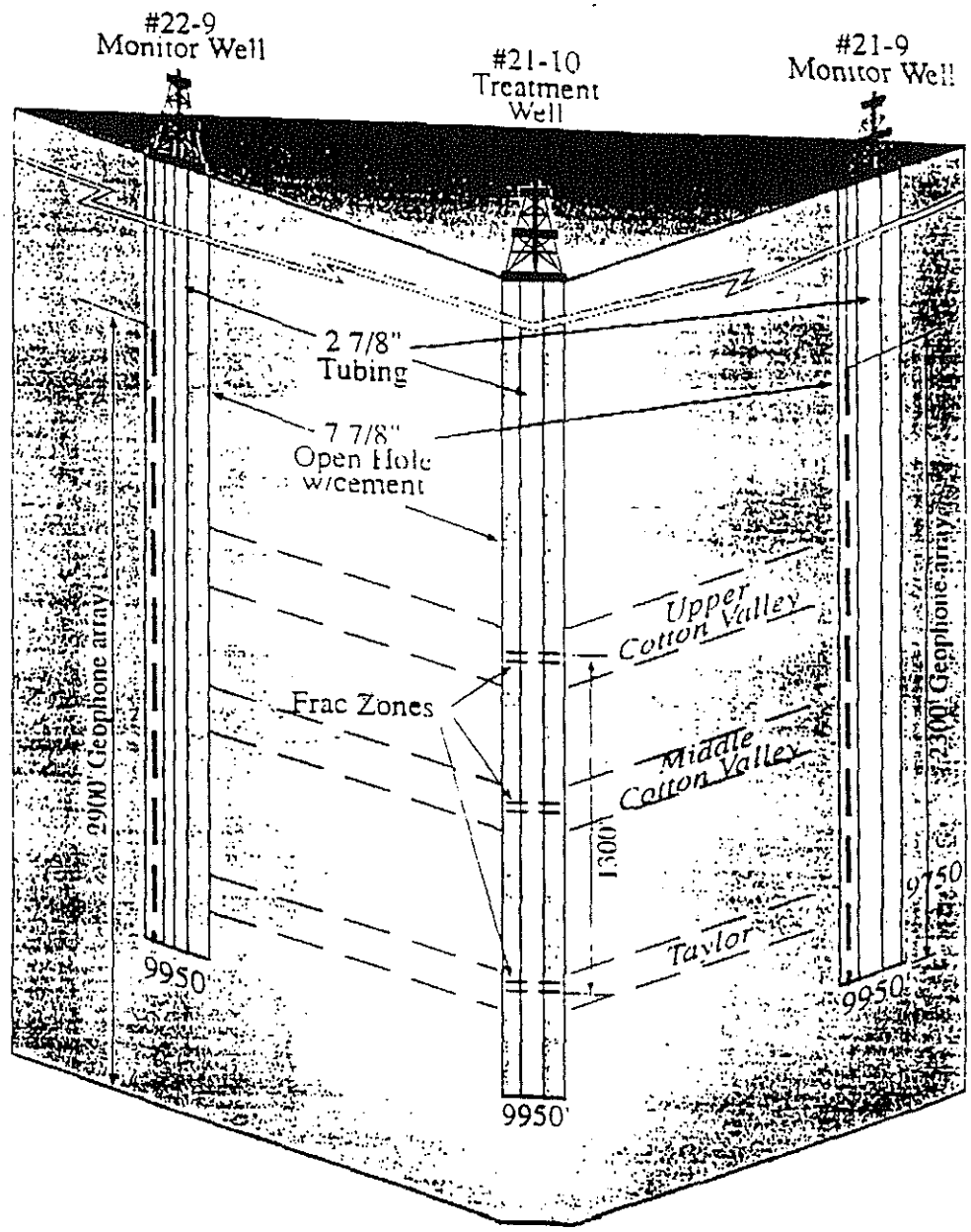

Figure 1: Schematic of a proposed UPRC hydraulic fracturing experiment in the Carthage Field, Panola County, Texas.

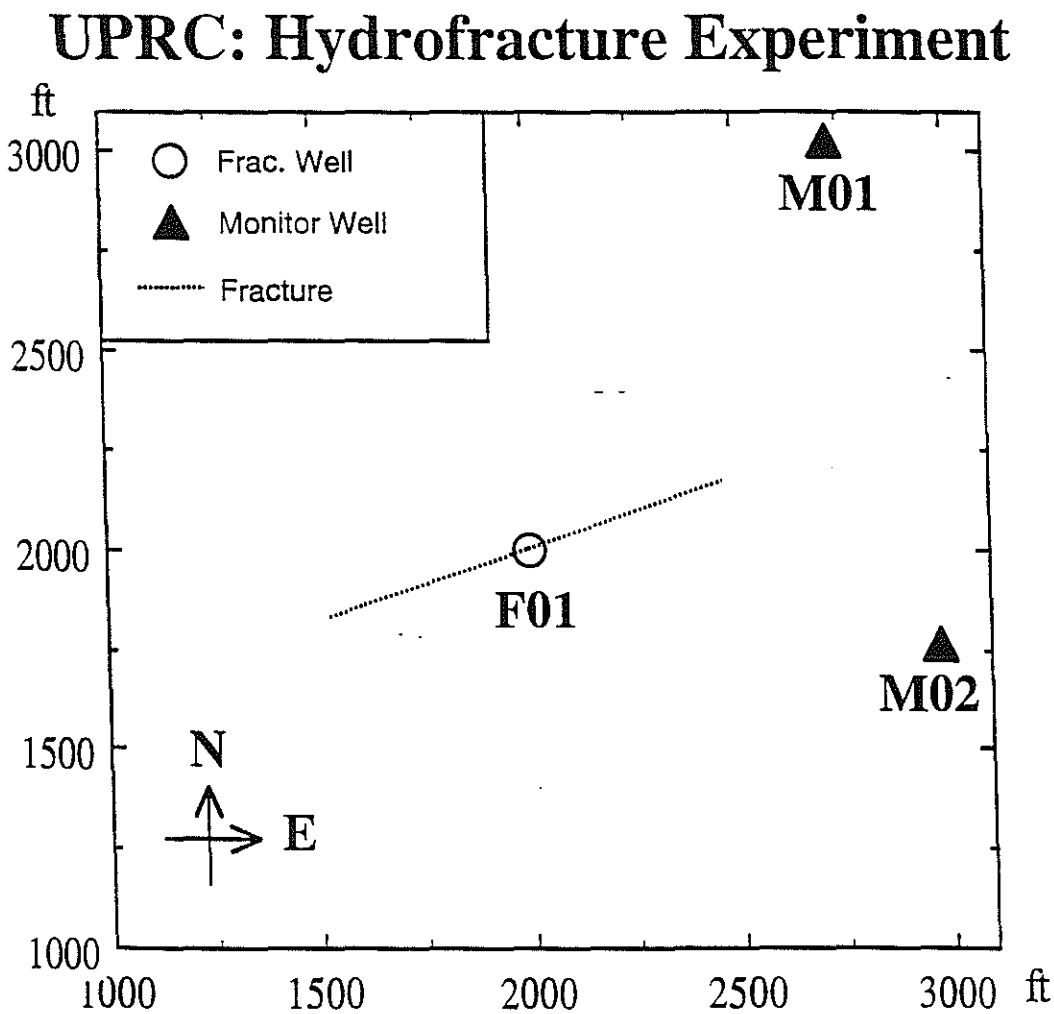

Figure 2: Plane view of the planned experiment area in Carthage Field showing the locations of a treatment well and two monitoring wells. The dashed line indicates an assumed azimuth of an expected hydraulic fracture.

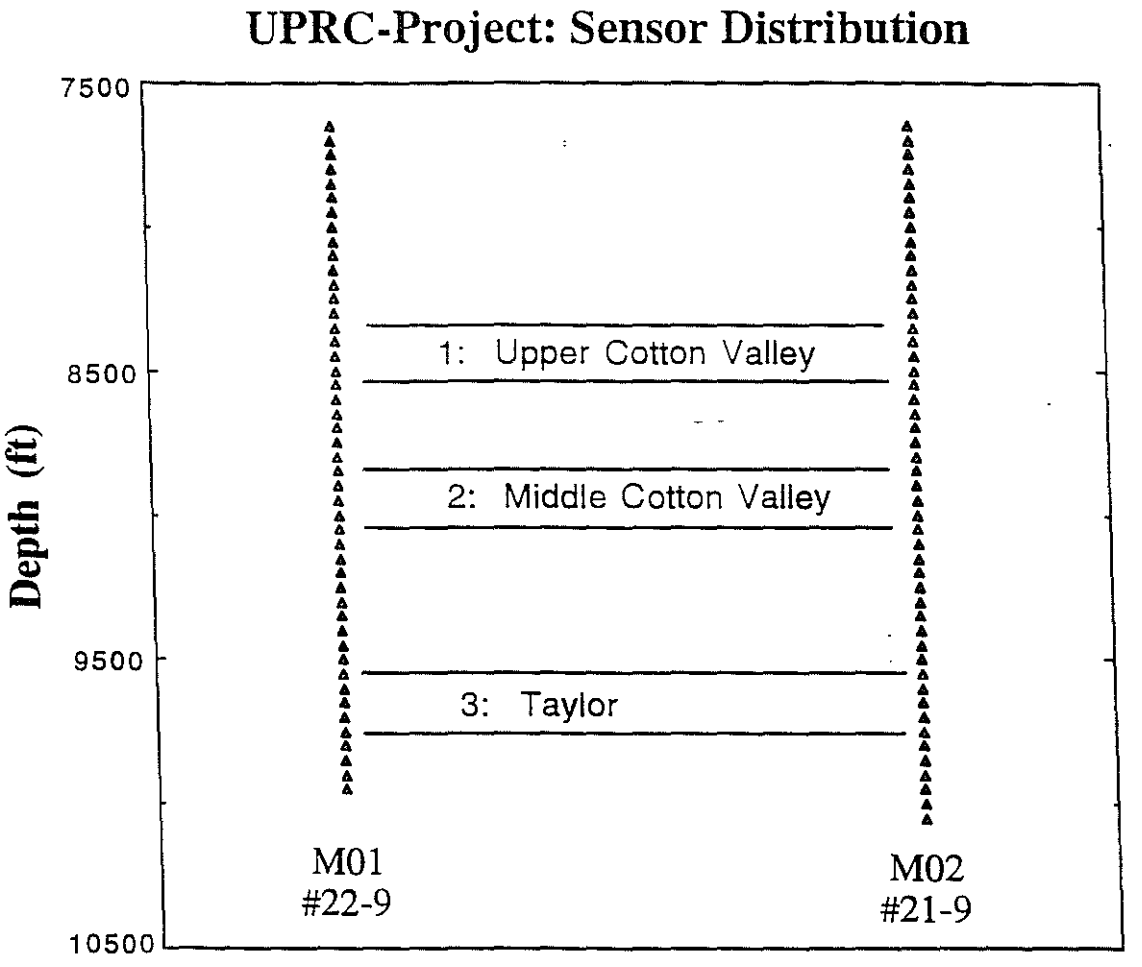

Figure 3: Cross-section of two monitor wells (M01=#22-9, M02=#21-9) at Carthage Field indicating the locations of seismometers and lithological units.

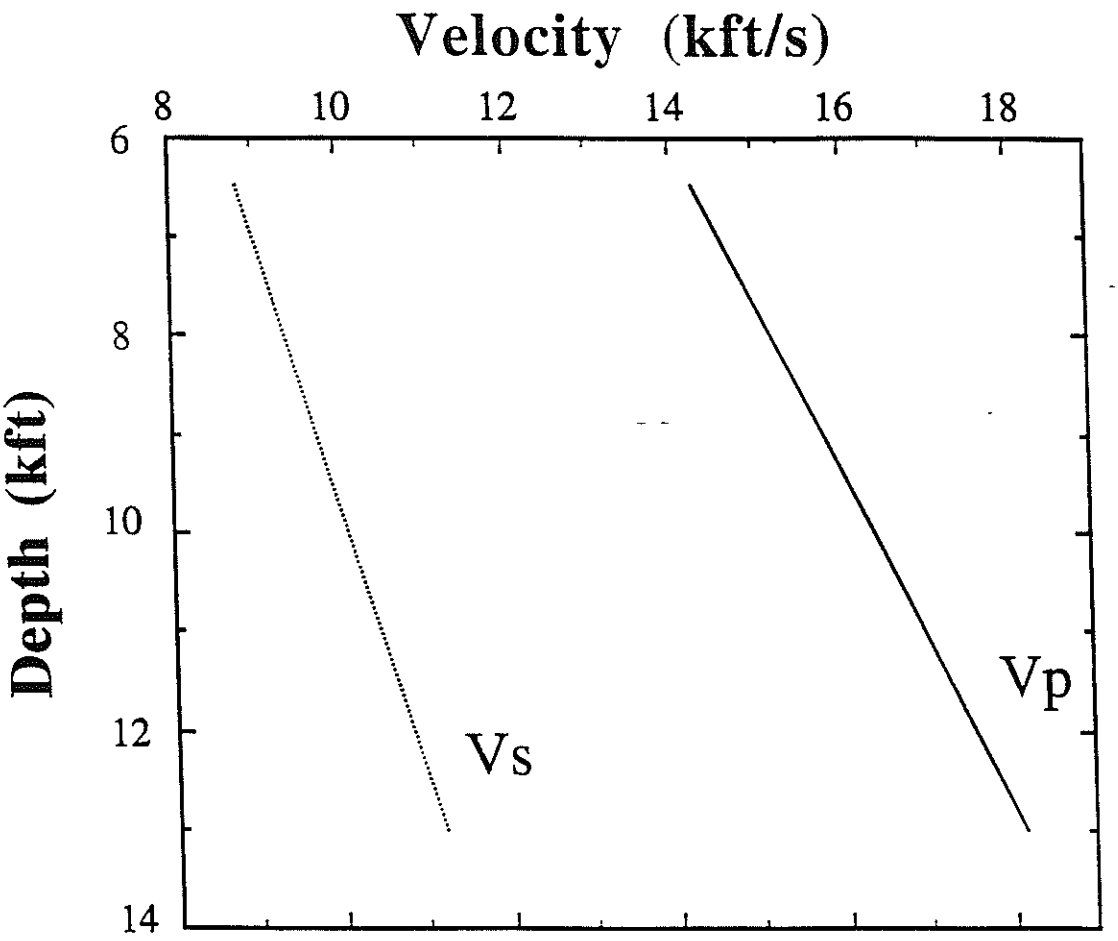

Figure 4: Linear gradient velocity models for P- and S-waves for the experimental site at Carthage Field.

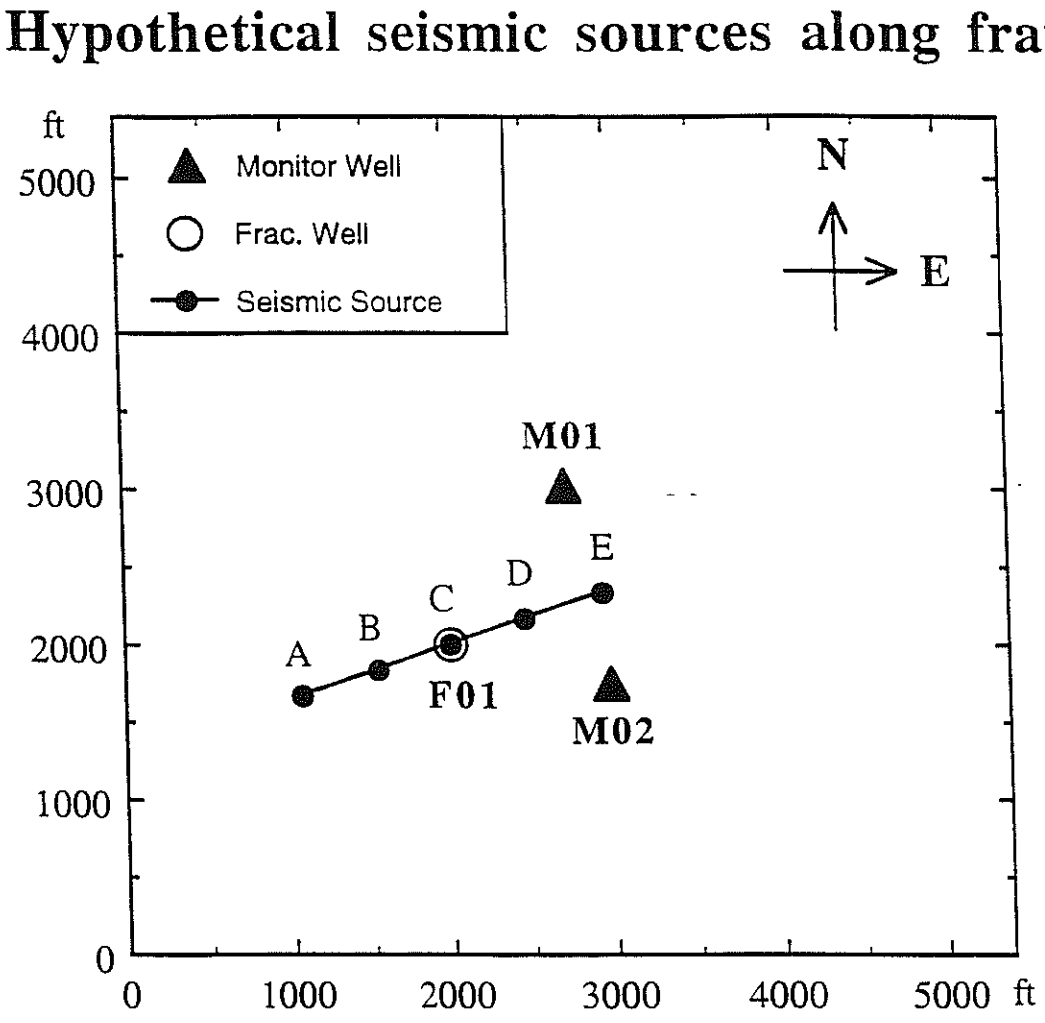

Figure 5: Map view showing the locations of one treatment well (open circle) and two monitor wells (triangles) and five hypothetical seismic sources (solid circles labeled with A, B, C, D, and E) along an expected strike of a hydraulic fracture zone.

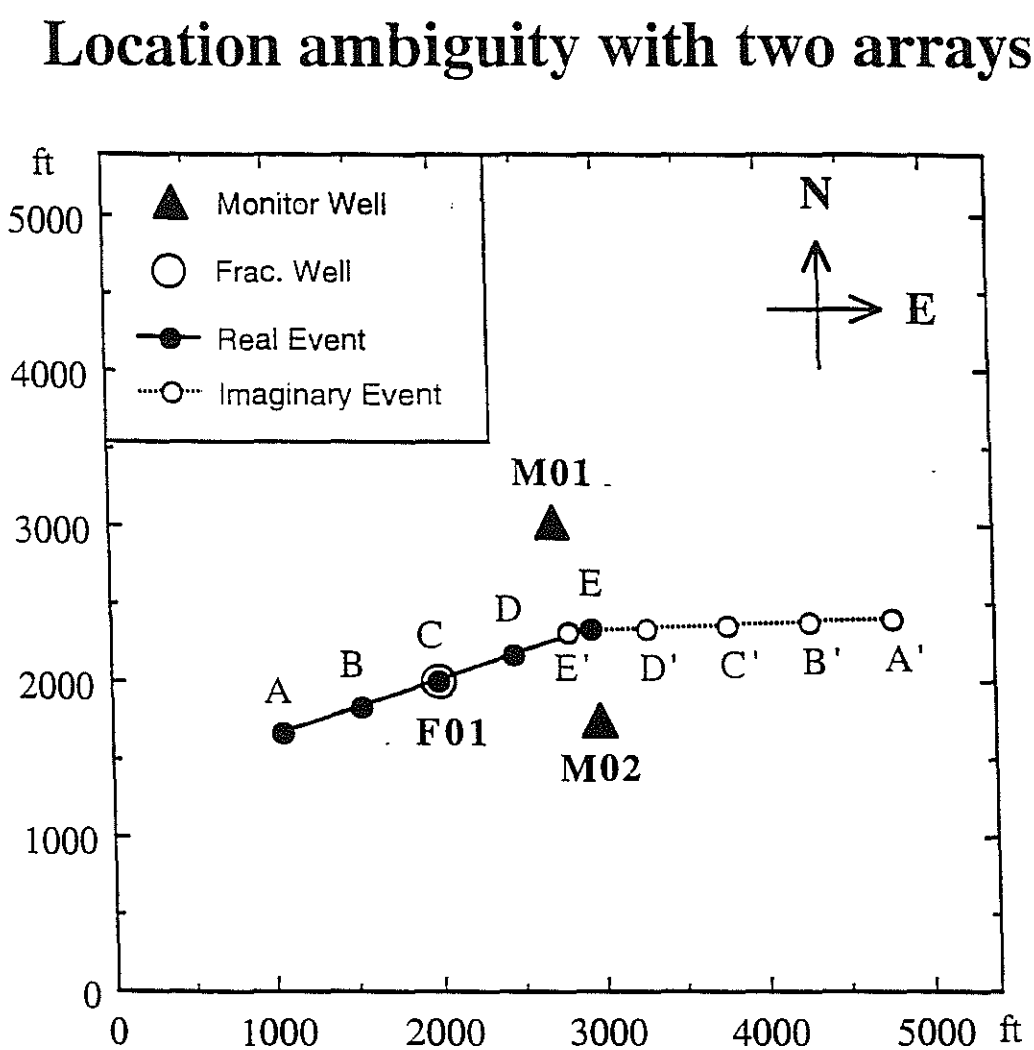

Figure 6: Map view showing the location ambiguity of five hypothetical seismic sources along the strike of an expected hydraulic fracture zone. Open circles connected with a dashed line represent ghost images of five hypothetical sources.

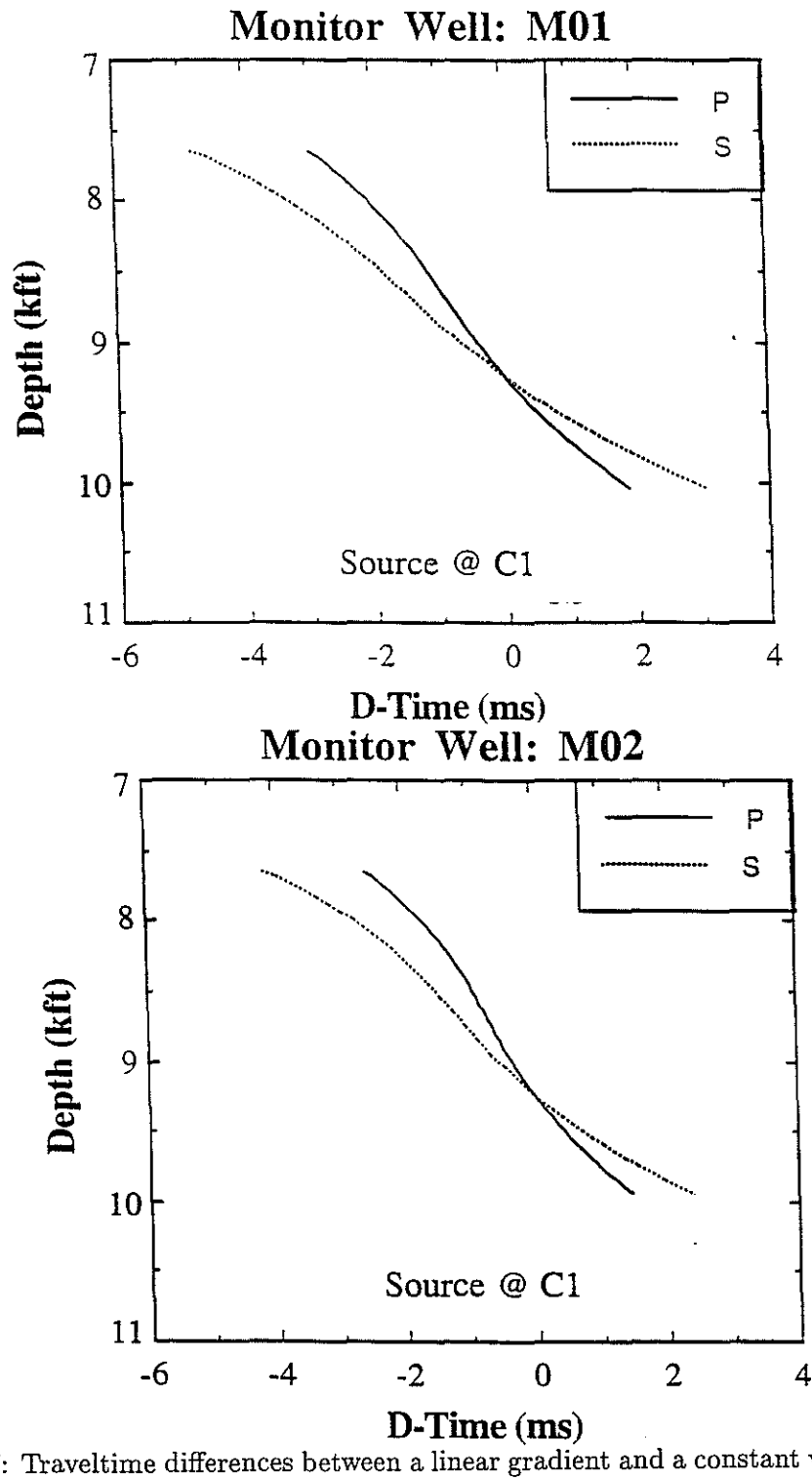

Figure 7: Traveltime differences between a linear gradient and a constant velocity model for a hypothetical seismic source (C1) at the Upper Cotton Valley to the two seismic arrays in the monitor wells.

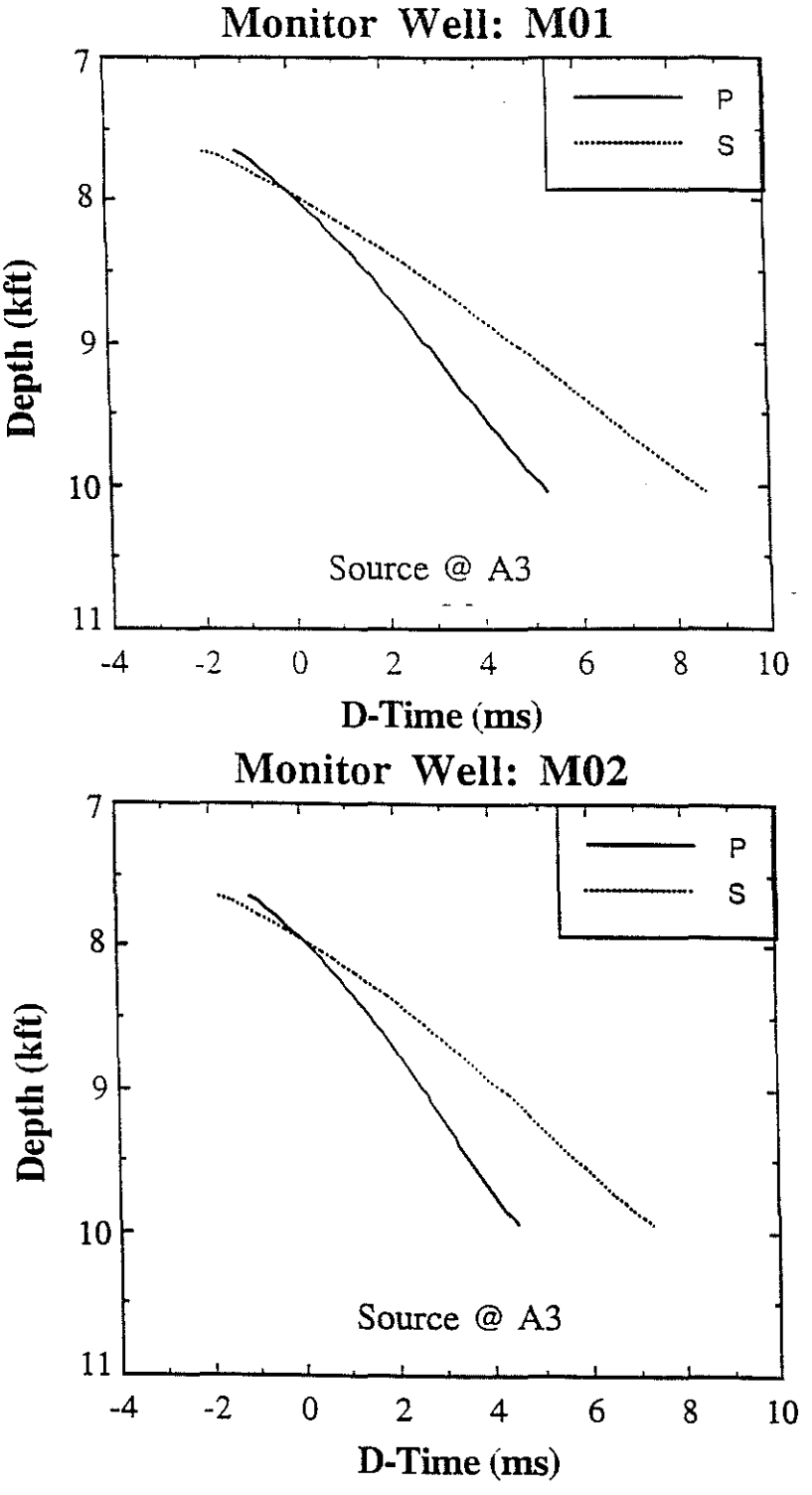

Figure 8: Traveltime differences between a linear gradient and a constant velocity model for a hypothetical seismic source in the layer of Taylor (A3) to the two seismic arrays.

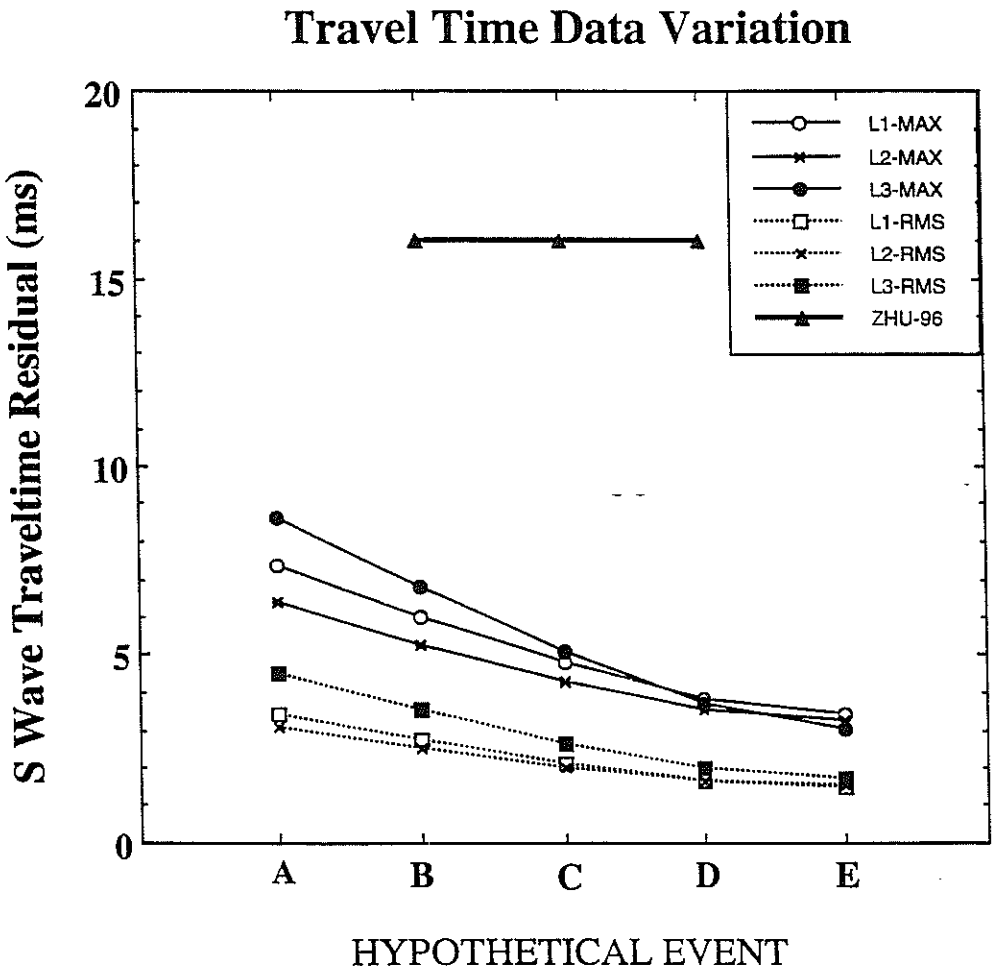

Figure 9: Comparison of the maximum and RMS (dashed lines) S-wave traveltime residuals for five sources at three different layers. The solid line with triangles is the error in traveltimes derived by Zhu *et al.* (1996).

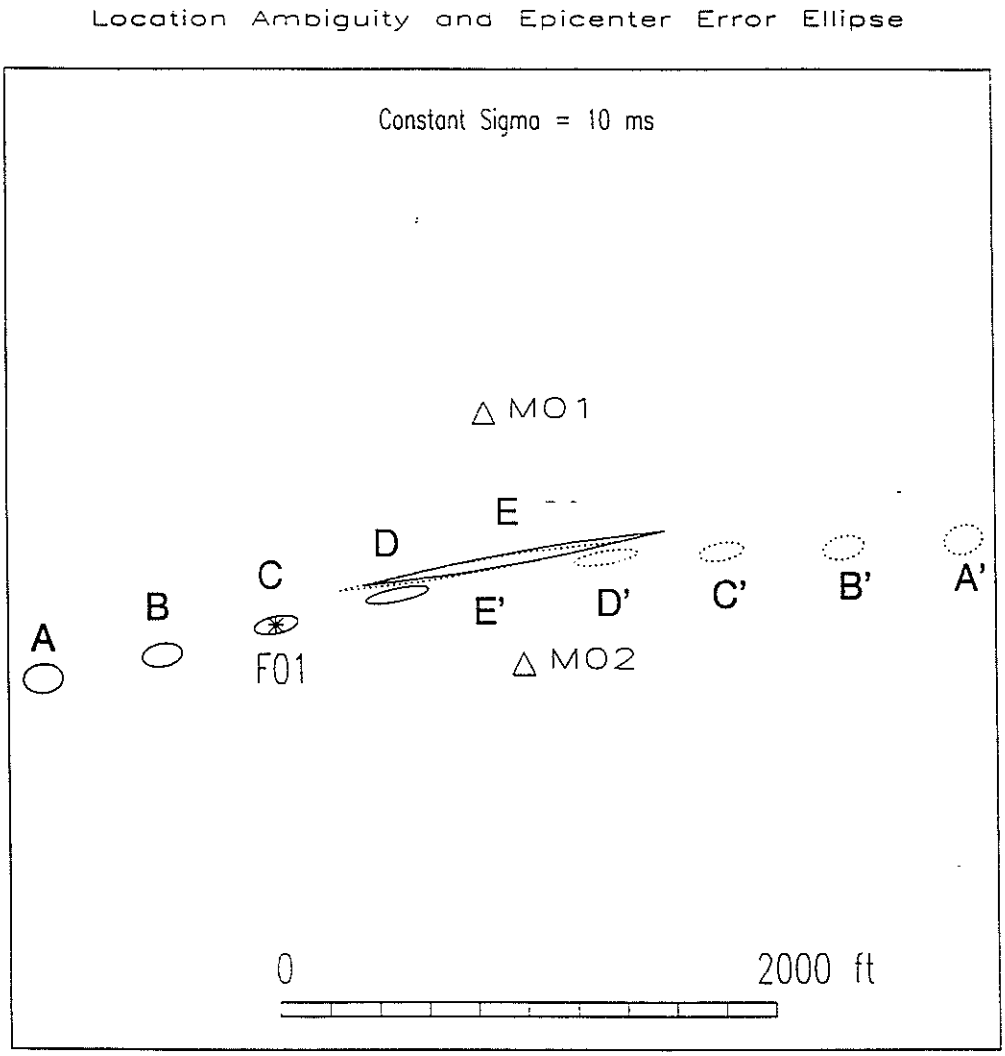

Figure 10: Absolute epicenter error ellipses, estimated with the constant σ model, for five hypothetical seismic sources at layer 2 along the assumed strike of the hydraulic fracturing zone and their ghost images. Note that the semimajor axes of error ellipses for sources E and E' are extremely large.

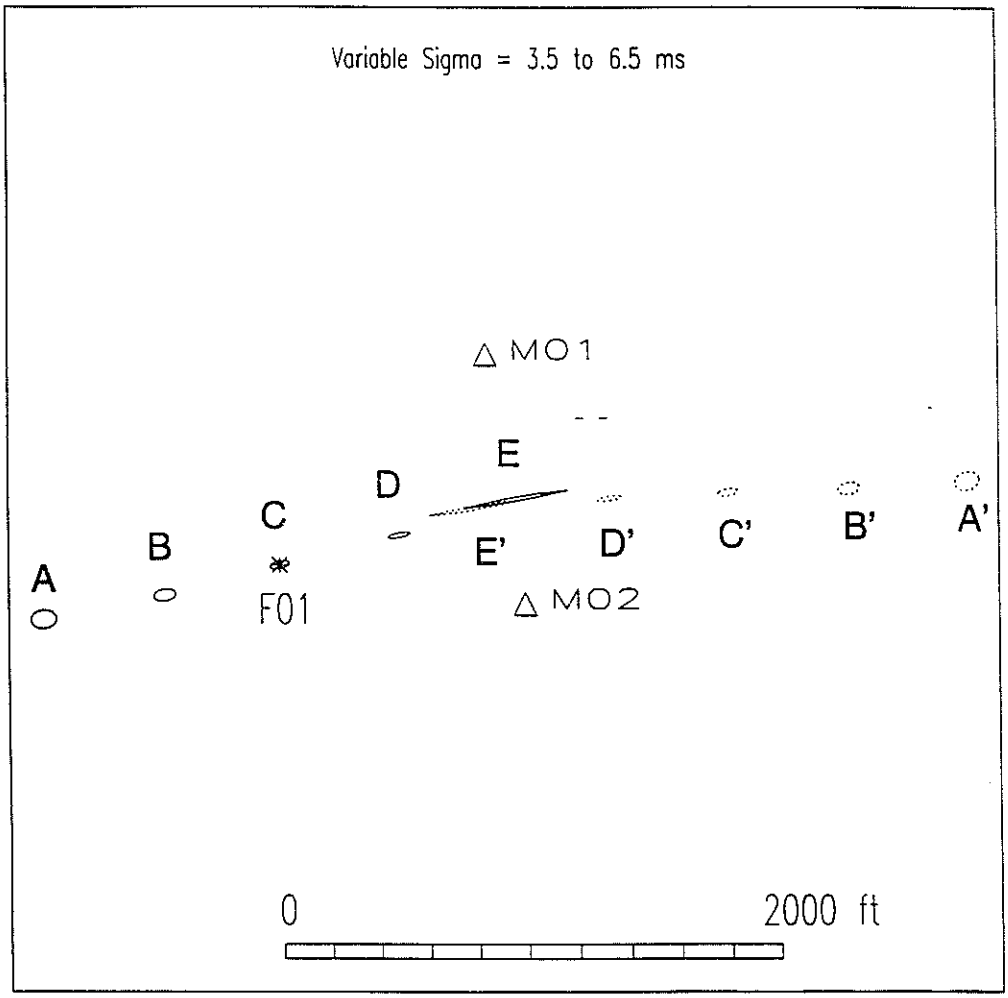

Figure 11: Absolute epicenter error ellipses, estimated with the variable σ model, for five hypothetical seismic sources at layer 2 along the assumed strike of the hydraulic fracturing zone and their ghost images. Note the difference in the error ellipses calculated with two different σ models.

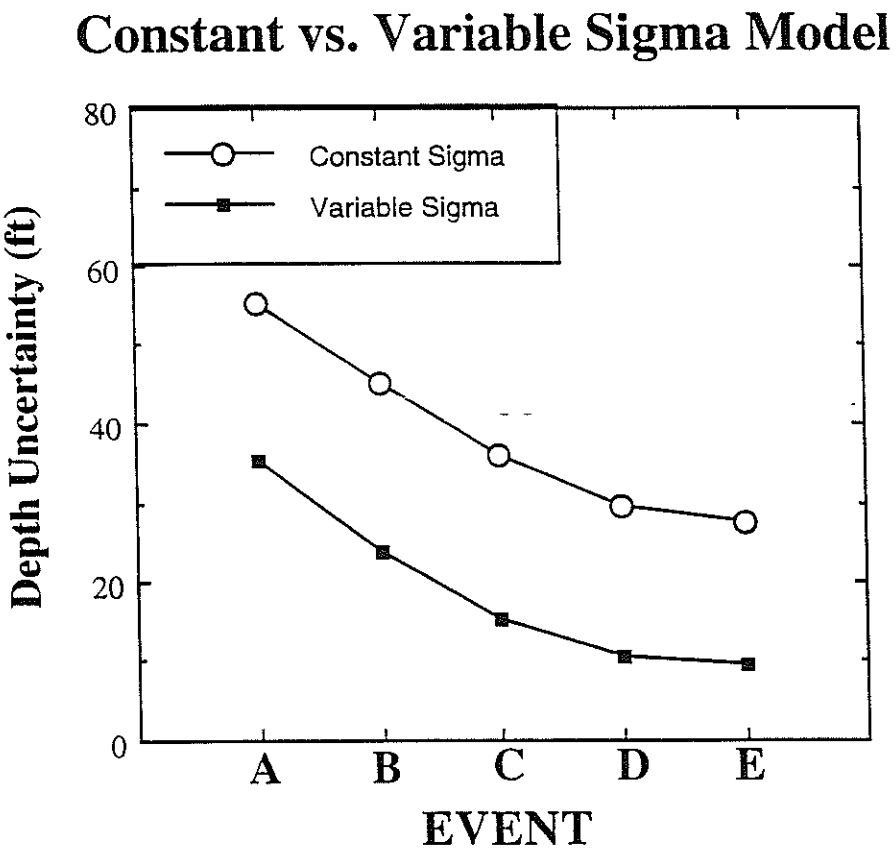

Figure 12: Absolute depth uncertainties estimated for five sources at layer 2 with two different σ models.

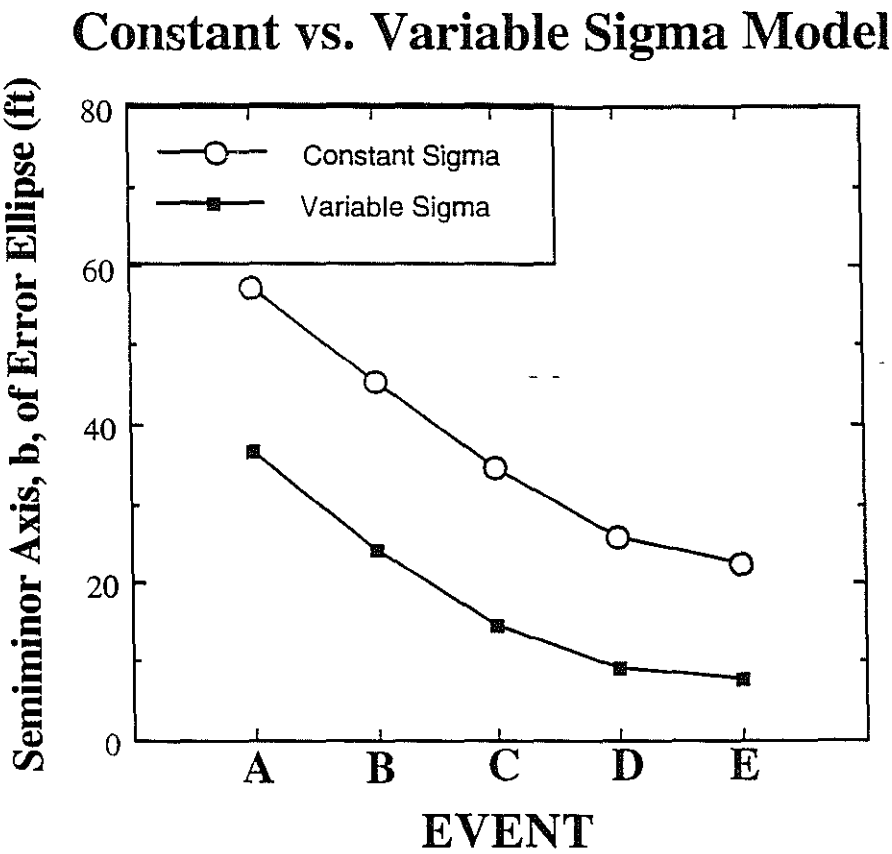

Figure 13: Absolute semiminor axes of error ellipses derived for five sources at layer 2 with two different σ models.

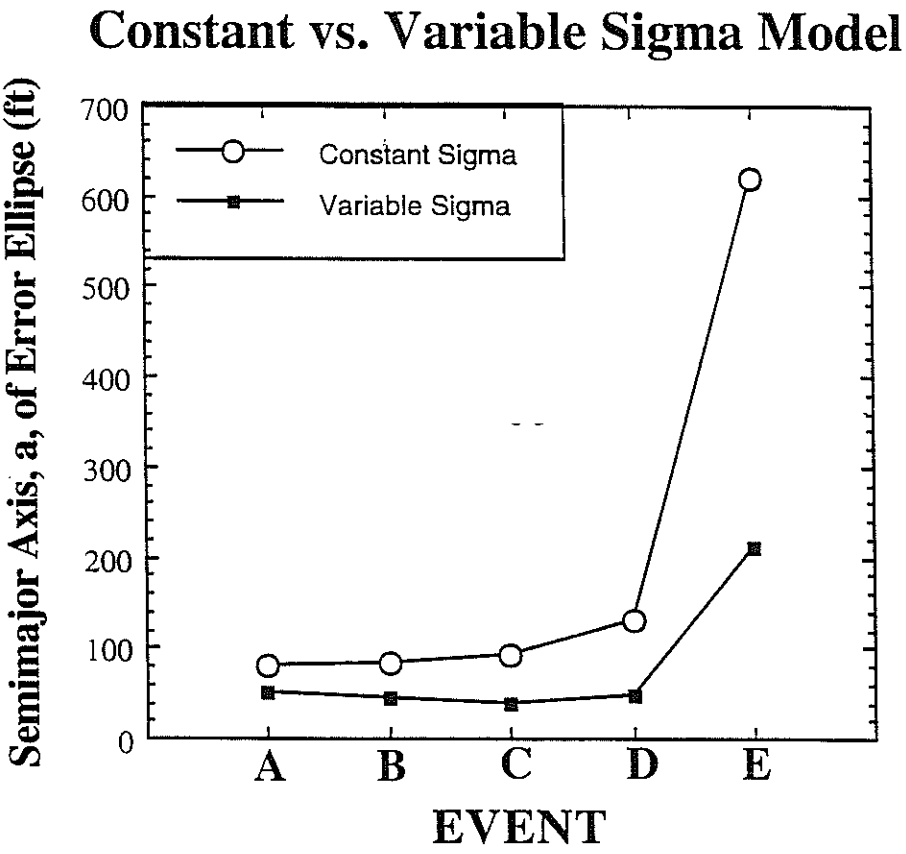

Figure 14: Absolute semimajor axes of error ellipses calculated for five sources at layer 2 with two different σ models.

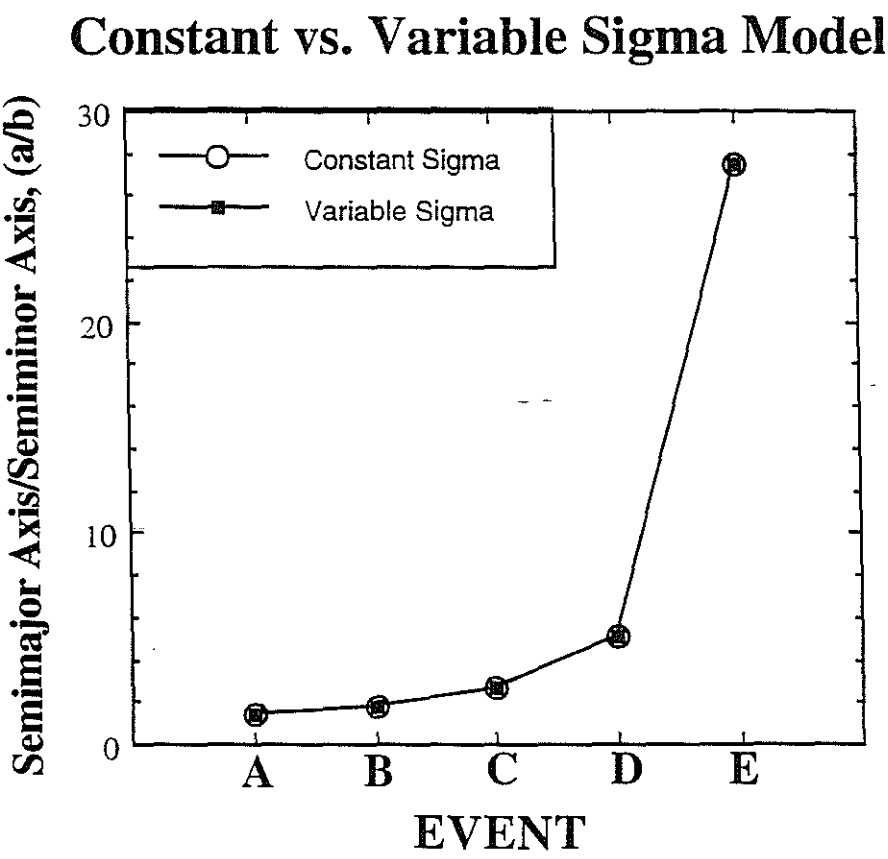

Figure 15: The ratio of absolute semimajor and seminminor axes of error ellipses are the same.

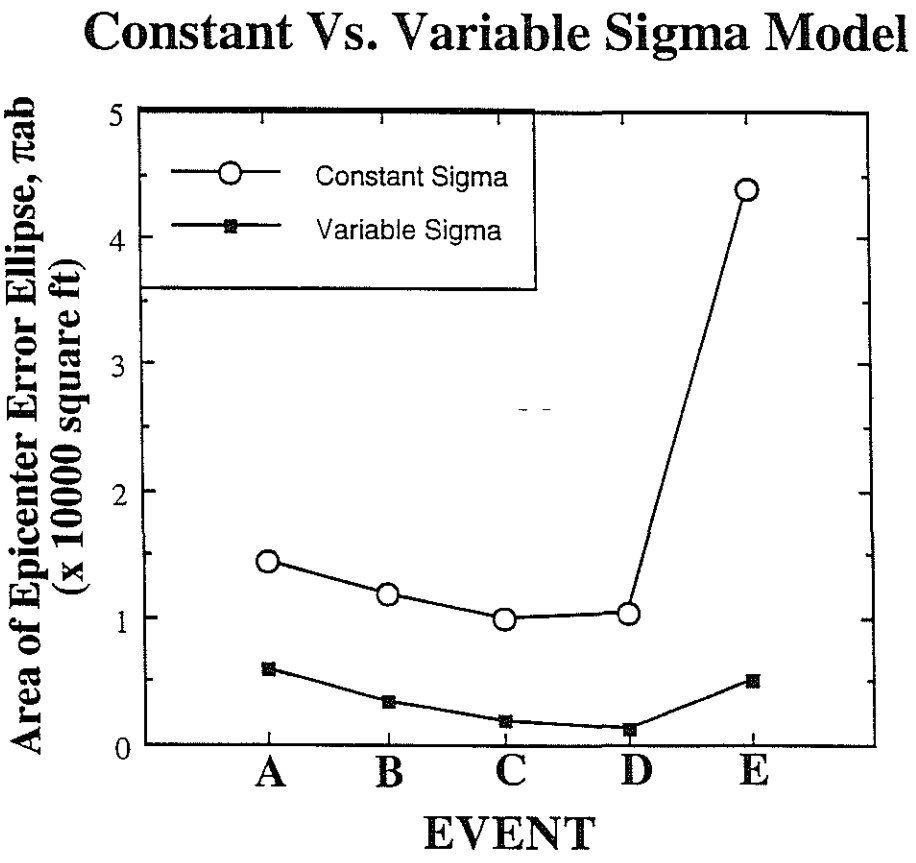

Figure 16: Comparison of the areas of the absolute error ellipses estimated with two different σ models. Note that the area of source D at layer 2 calculated with the variable σ model is the smallest.

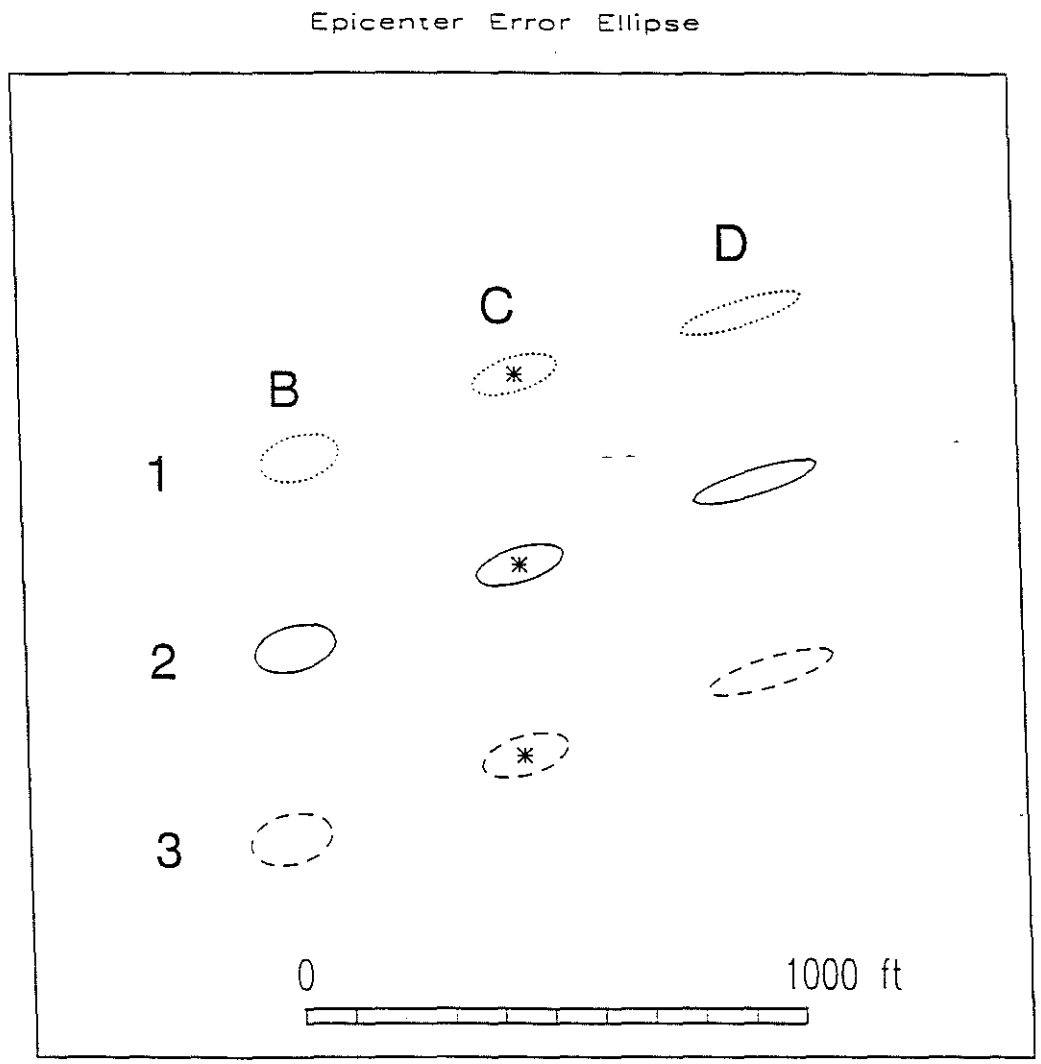

Figure 17: Comparison of absolute error ellipses for three hypothetical sources at B, C, and D with three different focal depths. Number 1, 2, and 3 represent the Upper, Middle Cotton Valley, and Taylor layers, respectively. Stars indicate the location of the injection well.

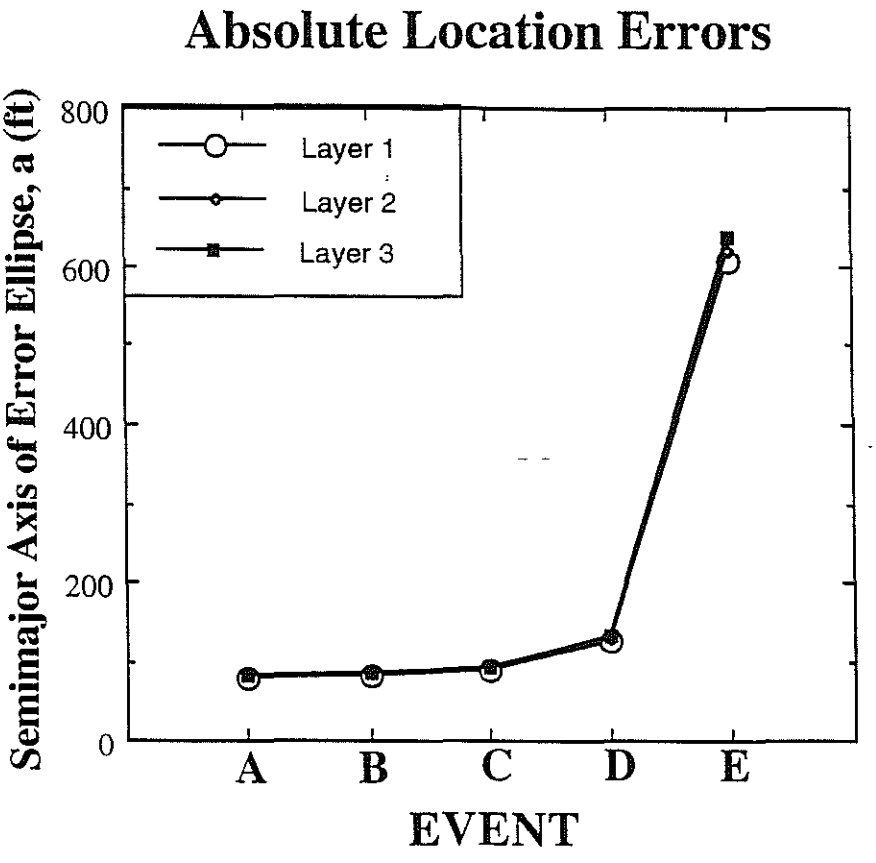

Figure 18: Semimajor axes of the absolute error ellipses for five hypothetical sources at three different layers. Note that the variation of the axes is not significant when the source depths change.

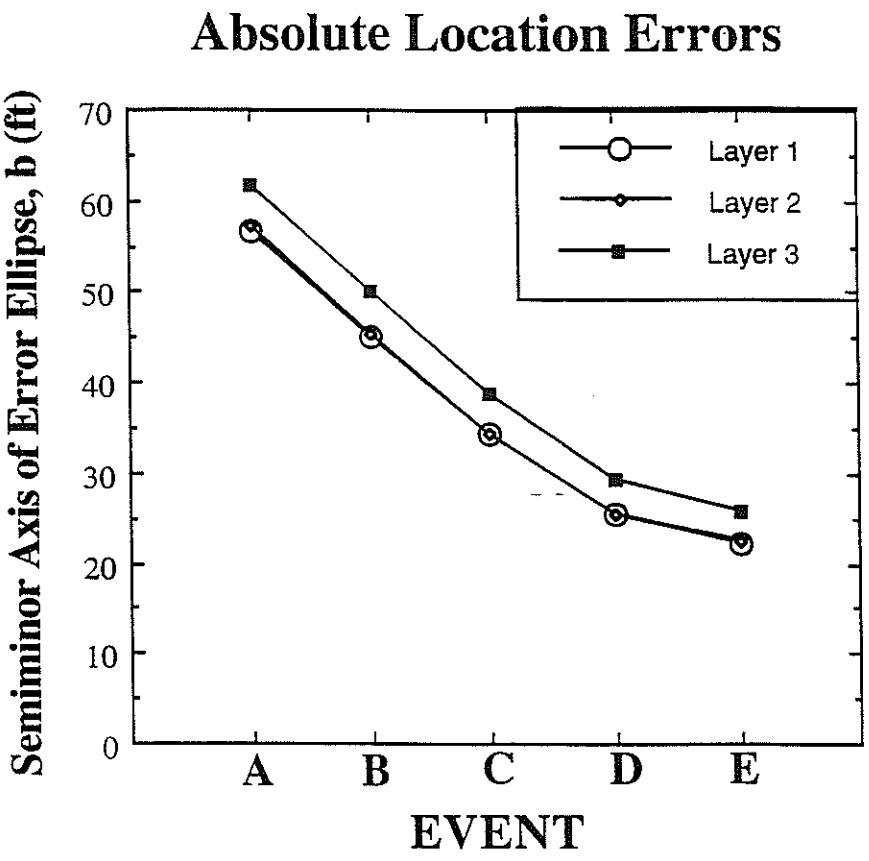

Figure 19: Semiminor axes of the absolute error ellipses for five hypothetical sources at three different layers. Note that the axes are largest for sources at layer 3 (Taylor).

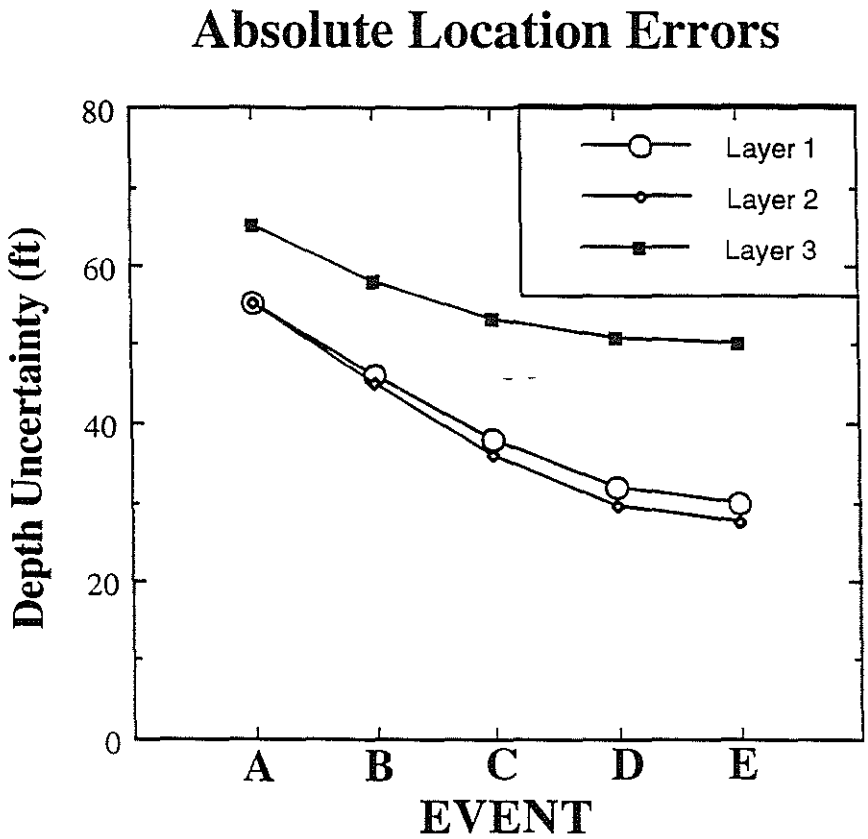

Figure 20: Absolute depth uncertainties for five sources at three layers. The largest depth uncertainties are for the sources in layer 3.

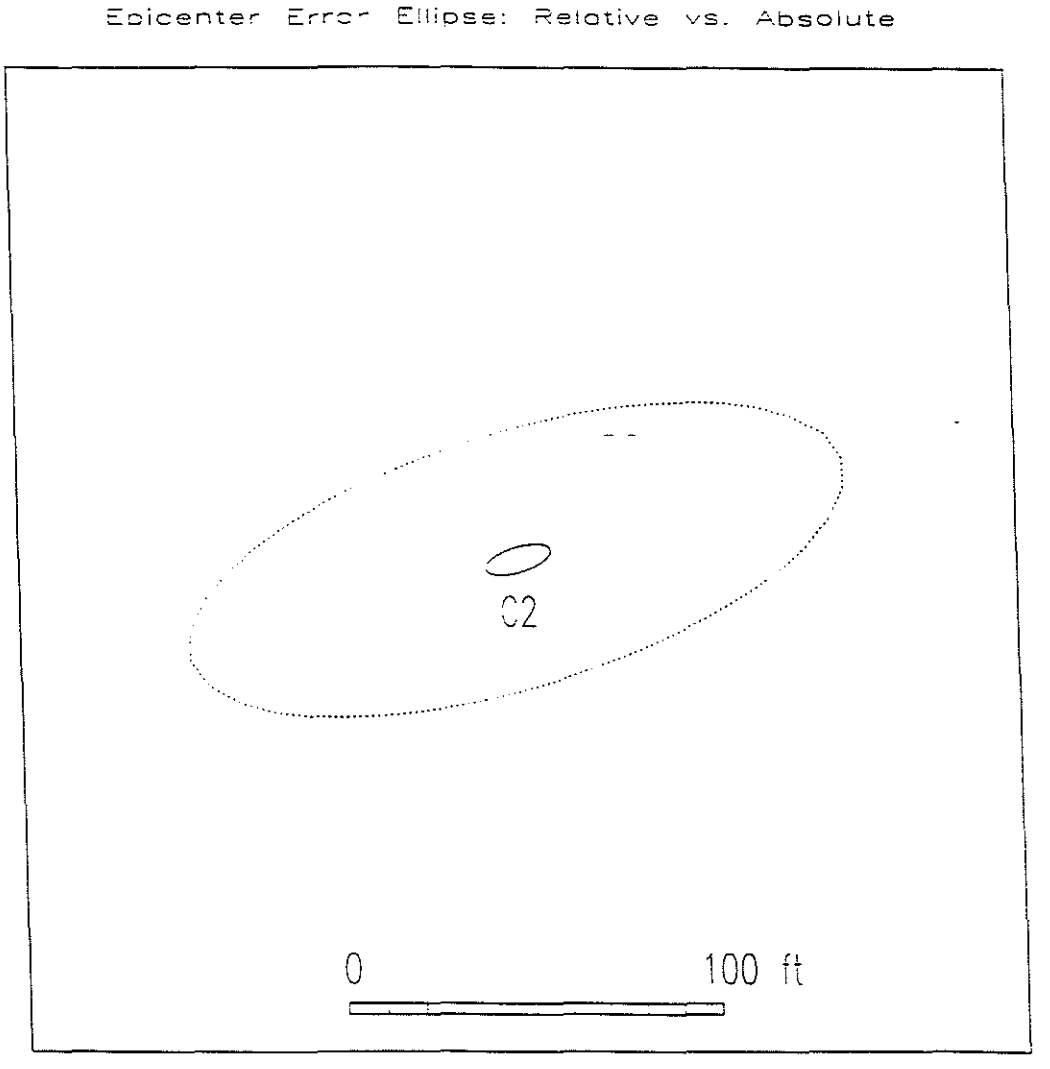

Figure 21: Relative (solid line) and absolute (dashed line) epicenter error ellipses for source C2.

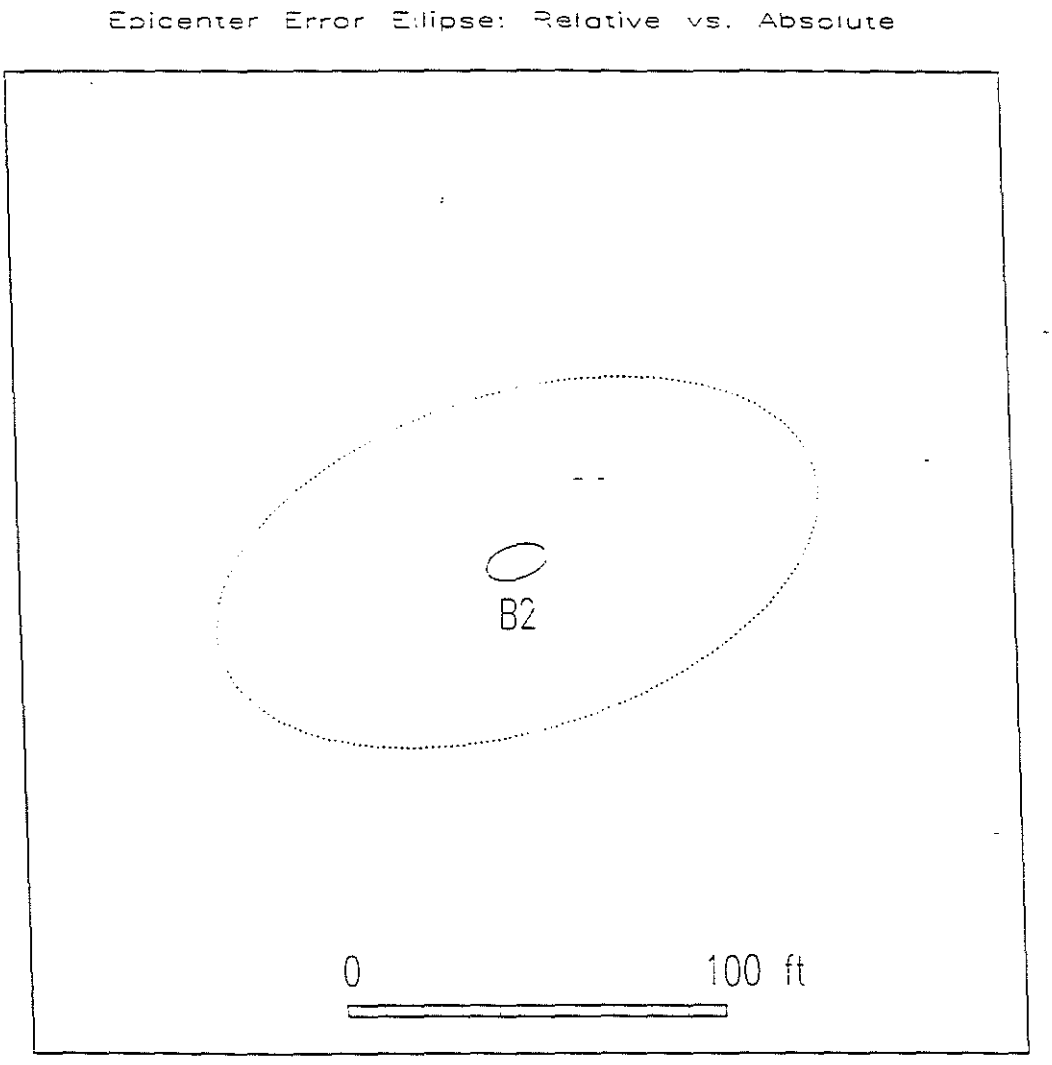

Figure 22: Relative (solid line) and absolute (dashed line) epicenter error ellipses for source B2.

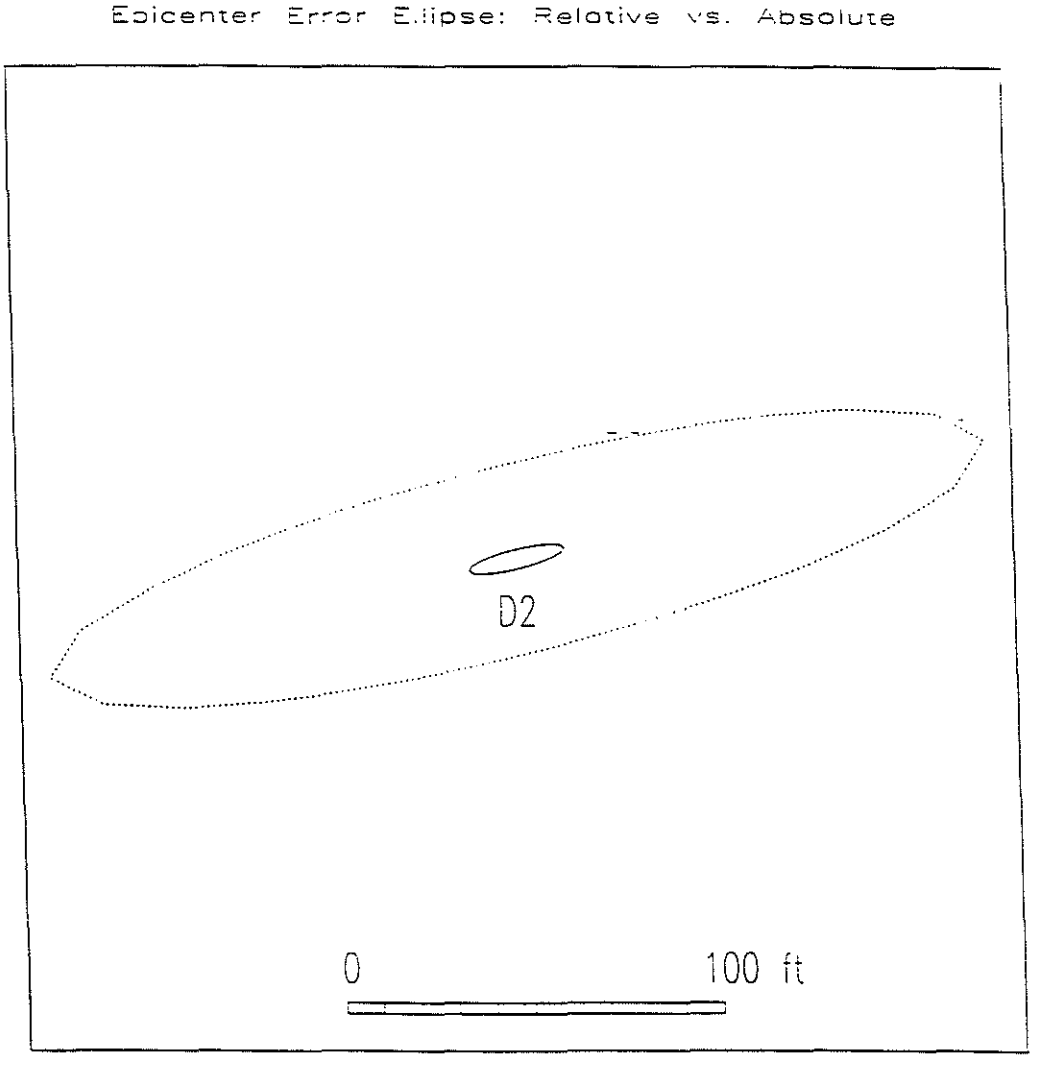

Figure 23: Relative (solid line) and absolute (dashed line) epicenter error ellipses for source D2.

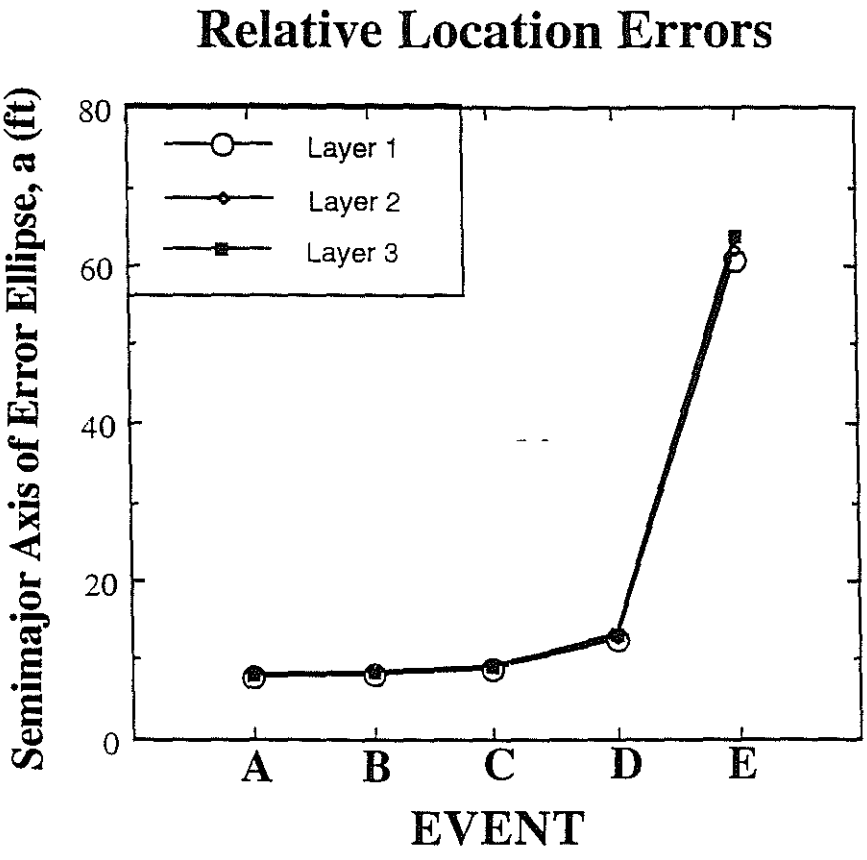

Figure 24: Semimajor axes of the relative error ellipses for five hypothetical sources at three different layers.

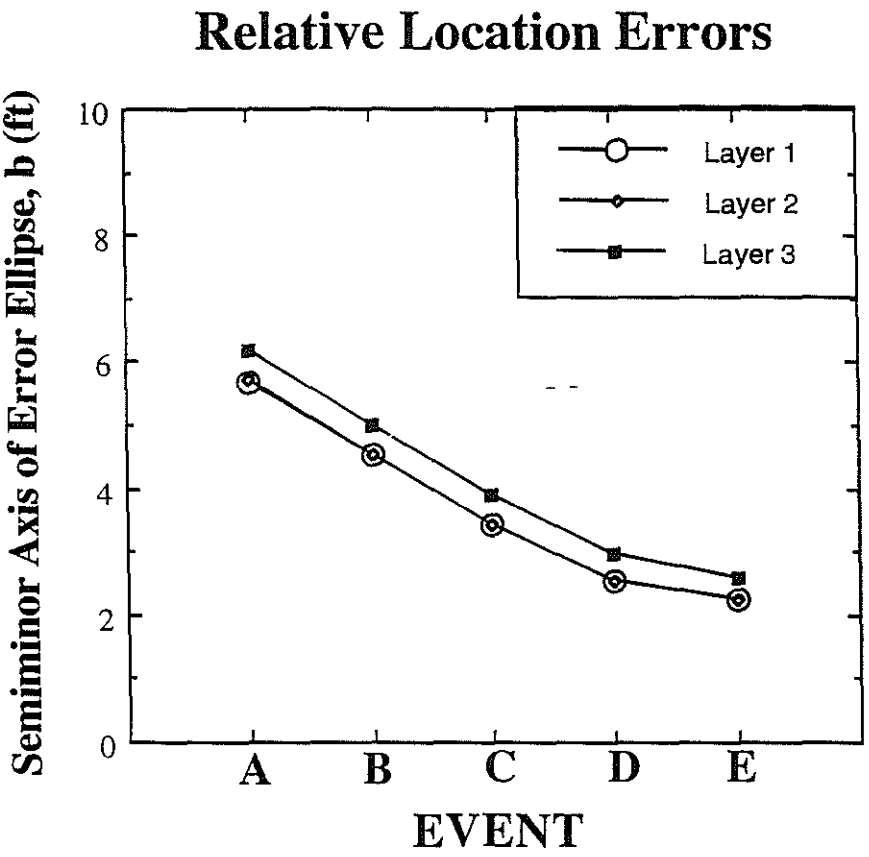

Figure 25: Semiminor axes of the relative error ellipses for five hypothetical sources at three different layers. Note that the axes are largest for sources at layer 3 (Taylor).

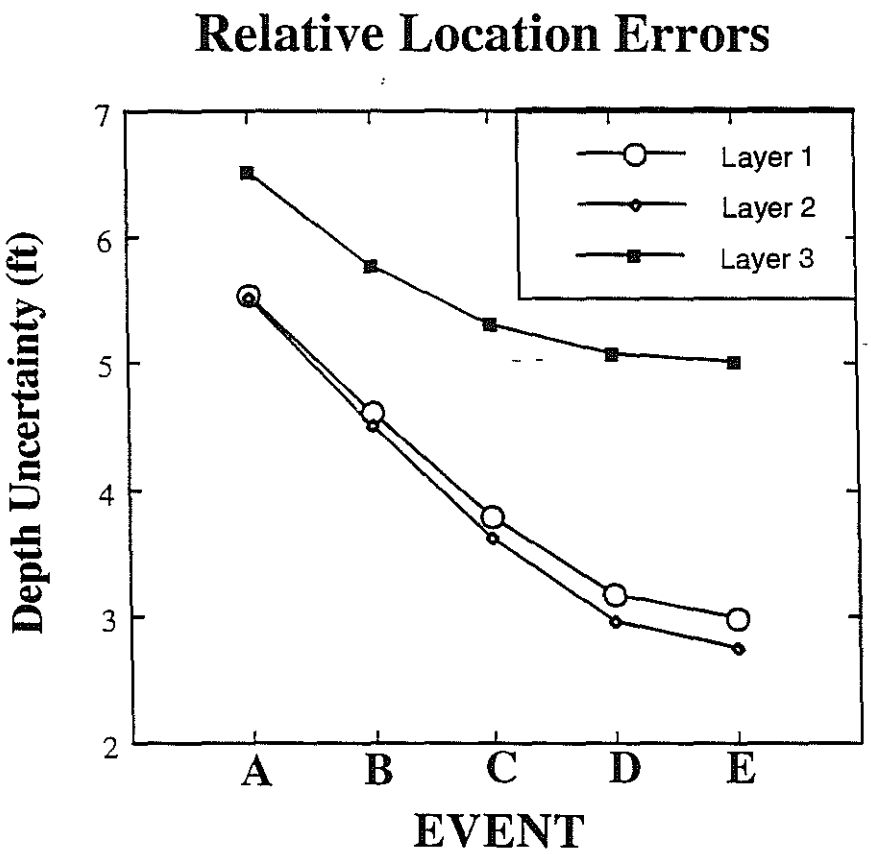

Figure 26: Relative depth uncertainties for five sources at three layers. The largest depth uncertainties are for the sources in the layer 3. Note the spatial variation of the relative depth uncertainties.

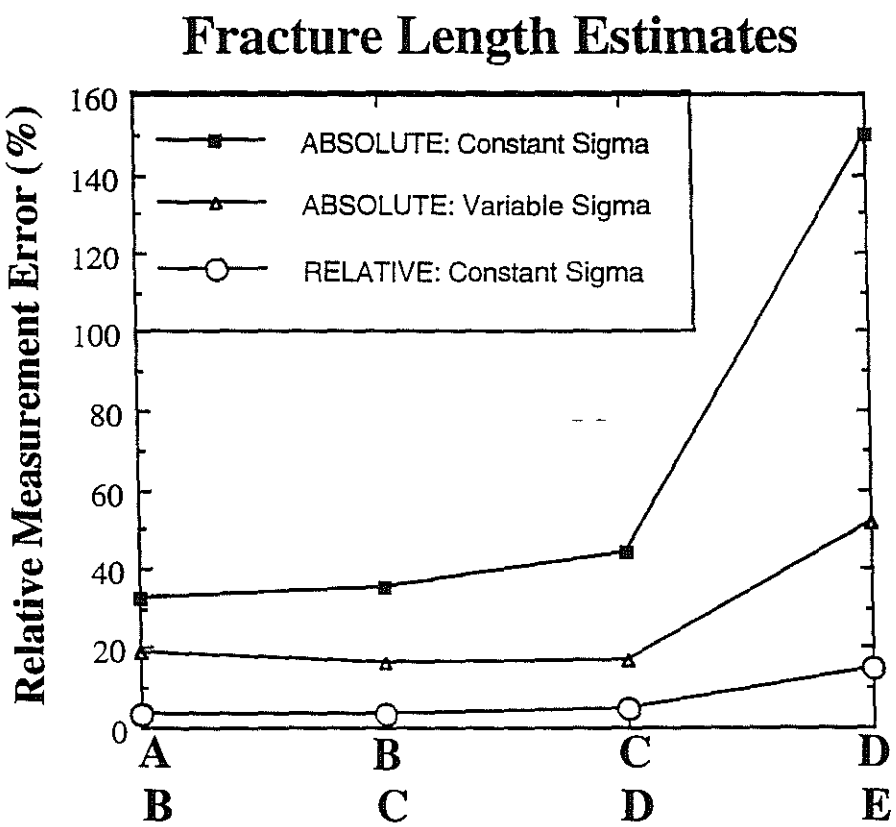

Figure 27: Relative measurement error for estimating the fracture length calculated with three different σ models. The smallest relative measurement error for the fracture length are obtained with the relative location results.